AN ABSTRACT OF THE THESIS OF

Michael W. Knapp for the degree of Master of Science in Chemical Engineering presented on June 15, 2012
Title: Continuous Flow Synthesis of Lead Sulfide and Copper Indium Diselenide Nanocrystals

Abstract approved:

Chih-Hung Chang

The use of size and shape tunable quantum confinement nanocrystals has many potential applications for use in semiconductors, optics and sensors. The synthesis of lead sulfide (PbS) and copper indium diselenide ($CuInSe_2$) nanoparticles are of particular interest for use in semiconductor, optoelectronics and bio-medical applications.

The continuous synthesis of lead sulfide (PbS) and copper indium diselenide ($CuInSe_2$) nanocrystals was undertaken in this work. Quality colloidal nanocrystal synthesis requires three components: precursors, organic surfactants and solvents. The synthesis of the nanocrystals can be thought of as a nucleation event, followed by a subsequent growth period. Both the nucleation and growth rates were found to be dependent upon factors such as temperature, growth time, and precursor concentration. For a continuous flow system the residence time (at nucleation and growth conditions) was also found to be important. In order to separate the nucleation and growth events, injection techniques were employed to achieve rapid nucleation of nanocrystals with final size dictated by the growth temperature and/or residence time through the growth zone of the reaction system.

Experimental parameters to investigate the size, shape, and composition of synthesized nanocrystals included injection temperature, growth temperature,

residence time, and concentration of organic surfactants. Size tunability was accomplished for both PbS and $CuInSe_2$ nanocrystals where particle sizes less than 10 nm were achieved and the resulting nanocrystal compositions were found to be at the approximate stoichiometric ratios for both PbS and $CuInSe_2$. The materials used for the process tubing and pumps were found to be important as chlorinated reaction byproducts were found to react with the stainless steel tubing and pump heads. Post processing was also found to be important in order to remove any possible reaction by-products and residual precursors from the surface of synthesized nanocrystals.

When at least one dimension of the nanocrystal approaches the exciton Bohr radius, the bandgap for the nanocrystal increases. UV-VIS spectroscopy was used to optically characterize synthesized PbS nanocrystals from our continuous flow synthesis. The absorption spectra for the particles demonstrated an absorption onset showing a large blueshift compared to that of bulk PbS. The blueshift matches closely with literature reports of the quantum confinement effect that would be desired when synthesizing PbS nanoparticles at diameters that are less than the PbS exciton Bohr radius of 18 nm.

Continuous Flow Synthesis of Lead Sulfide and Copper Indium Diselenide Nanocrystals

by
Michael W. Knapp

A THESIS

submitted to

Oregon State University

in partial fulfillment of
the requirements for the
degree of

Master of Science

Presented June 15, 2012
Commencement June 2013

Master of Science thesis of Michael W. Knapp presented on June 15, 2012.

APPROVED:

Major Professor, representing Chemical Engineering

Head of the School of Chemical, Biological and Environmental Engineering

---

Dean of the Graduate School

I understand that my thesis will become part of the permanent collection of Oregon State University libraries. My signature below authorizes release of my thesis to any reader upon request.

Michael W. Knapp, Author

ACKNOWLEDGEMENTS

Firstly, I want to thank my advisor, Dr. Chih-Hung Chang for the opportunities he provided me by bringing me into his research group. His guidance helped me to develop skills that will be valuable throughout my career.

I would also like to thank my committee members: Dr. Brian K. Paul, Dr. Gregory S. Herman and Dr. Kaichang Li.

Additionally I would like to thank Teresa Sawyer and Dr. Yi Liu at the Oregon State University Electron Microscope Facility for their assistance with TEM and SEM/EDX characterization. At the University of Oregon's Center for Advanced Materials Characterization in Oregon facility, I would like to thank Josh Razink for his assistance with using their HRTEM. I would also like to thank Voxtel's Nanotechnology Products Group for their guidance on using optical characterization, and willingness in answering questions. Thanks also go to MBI for providing lab space and to Brendan Flynn for assistance with Raman spectroscopy. I would like to thank Dr. Ki-Joong Kim and Peter Kreider for their assistance. Funding provided by the Department of Energy's Office of Energy Efficiency and Renewable Energy Industrial Technology Program, Nanomanufacturing Activity through award number NT08847 DOE ITP ONAMI-GAP fund and Voxtel, Inc. is appreciated.

The continued assistance and mentorship provided by Dr. Nick Wannenmacher is also greatly appreciated.

Lastly, I would like to thank my family and friends for their continued support throughout my research and studies.

Michael W. Knapp

TABLE OF CONTENTS

Page

Chapter 1. INTRODUCTION 1

Chapter 2. LITERATURE REVIEW AND BACKGROUND 3

2.1 Quantum Confinement Effect 3

2.2 Colloidal Nanocrystal Synthesis 4

2.2.1 General Understanding of Nucleation and Growth Mechanism 4
2.2.2 Reaction Pathways of $CuInSe_2$ and PbS Colloidal Nanocrystals 6
2.2.3 Crystal Structures 7
2.2.4 Synthesis Parameters 10

Chapter 3. MATERIALS AND RESEARCH METHODS 12

3.1 Synthesis Methods 12

3.2 Materials 12

3.3 Precursors Preparation and Synthesis 13

3.3.1 TOPSe Precursor 13
3.3.2 Precursor of Cu+In with OA/TOP 13
3.3.3 $CuInSe_2$ Synthesis 14
3.3.4 Lead Oleate Precursor 14
3.3.5 Sulfur Precursor 14
3.3.6 PbS Synthesis 15
3.3.7 Experimental Setup 15
3.3.8 Post-Processing 16

3.4 Characterization of Materials 16

3.4.1 Transmission Electron Microscopy (TEM) 16
3.4.2 X-Ray Diffraction (XRD) 17
3.4.3 Energy Dispersive Spectroscopy (EDS) 18
3.4.4 UV-Vis and Photoluminescence (PL) 18
3.4.5 Raman Spectroscopy 19

Chapter 4. ANALYSIS AND DISCUSSION OF RESULTS 20

4.1 $CuInSe_2$ Synthesis 20

TABLE OF CONTENTS (Continued)

Page

4.2 PbS Synthesis 41

Chapter 5. CONCLUSIONS 64

5.1 Current state of topic research synthesis 64

5.2 Summary of motivation for topic research 64

5.3 Results and recommendations of PbS and $CuInSe_2$ 65

5.4 Future Development Recommendations 67

BIBLIOGRAPHY 69

LIST OF FIGURES

Figure Page

2.1 PbS face-centered cubic crystal structure. 8

2.2 Body-centered tetragonal $CuInSe_2$ chalcopyrite. 9

2.3 Face-centered cubic $CuInSe_2$ sphalerite. 9

3.1 General experimental setup. 16

4.1 XRD analysis of run 1 indicating $CuInSe_2$ characteristic peaks with intermediates present. 22

4.2 XRD of run 2 indicating $CuInSe_2$ characteristic peaks. 24

4.3 XRD of run 3 showing reduced intensity at increased growth temperatures for $CuInSe_2$. 25

4.4 XRD of run 4 indicating broad $CuInSe_2$ characteristic peaks and lack of intermediate peaks. 26

4.5 Large agglomeration of $CuInSe_2$ nanocrystals at 215°C growth and 8 minute residence time. 28

4.6 HRTEM with overlapping $CuInSe_2$ nanocrystals at 215°C growth and 8 minute residence time. 28

4.7 Agglomerated $CuInSe_2$ nanocrystals with distinct single crystals from run 5. 30

4.8 HRTEM of agglomerated of $CuInSe_2$ nanocrystals from run 5. 30

4.9 XRD showing characteristic peaks for $CuInSe_2$ for run 5. 31

4.10 As-synthesized $CuInSe_2$ nanocrystals from run 5. 32

4.11 $CuInSe_2$ nanocrystals using a triple-wash and sonication method from run 5. 32

4.12 XRD of run 6 with increasing intensity of characteristic $CuInSe_2$ peaks. 34

4.13 Raman results for injection temperature at 250°C and 8 minute residence time from run 6. 35

4.14. TEM image of dispersed particles for run 6. 37

4.15 HRTEM and FFT of dispersed particle from run 6. 37

4.16 Size distribution histogram for particles from run 6. 38

LIST OF FIGURES (Continued)

Figure Page

4.17 TEM image of agglomerated particles for run 6. 38
4.18 SAED of agglomerated particles from run 6. 39
4.19 TEM of polymorph dispersed particles for run 7. 40
4.20 XRD run 1 with characteristic PbS peaks. 44
4.21 TEM image of PbS nanocrystals for run 1 at a 5 minute residence time. 45
4.22 TEM image of PbS nanocrystals for run 1 at a 2.5 minute residence time. 46
4.23 XRD of run 2 with characteristic PbS peaks. 47
4.24 TEM image of PbS nanocrystals from run 2 at a 100°C growth temperature. 48
4.25 Run 2 size distribution of PbS particles grown at 100°C. 48
4.26 HRTEM of PbS nanocrystals synthesized at 100°C from run 2. 50
4.27 HRTEM and FFT image of PbS nanocrystal grown at 100°C growth from run 2. 51
4.28 EDS of PbS material from run 2. 51
4.29 TEM image of PbS nanocrystals for run 3 at 100°C. 53
4.30 TEM image of PbS nanocrystals of run 3 at 120°C. 54
4.31 Run 3 size distribution of PbS particles grown at 100°C. 54
4.32 Run 3 size distribution of PbS particles grown at 120°C. 55
4.33 HRTEM of PbS nanocrystals synthesized in run 3 at 100C°. 55
4.34 Close up of PbS nanocrystal circled in black in Figure 4.34. 56
4.35 UV-Vis and PL results of PbS nanocrystals from run 3. 57
4.36 Fitted absorbance data for determining bandgap energy for run 3. 58
4.37 TEM image of PbS nanocrystals at 90°C from run 4. 60
4.38 TEM image of PbS nanocrystals 120°C from run 4. 60
4.39 Run 4 size distribution of PbS particles grown at 90°C. 61
4.40 Run 4 size distribution of PbS particles grown at 120°C. 61

LIST OF FIGURES (Continued)

Figure Page

4.41 UV-Vis results of particles synthesized for run 4. 62

4.42 Fitted absorbance data for determining bandgap energy when assuming absorbance is zero. 63

LIST OF TABLES

Table		Page
4.1	$CuInSe_2$ synthesis runs.	21
4.2	EDX results indicating increased In_2Se_3 crystal dissolution and formation into the $Cu_xIn_ySe_z$ crystal structure.	33
4.3	PbS synthesis runs.	43

Continuous Flow Synthesis of Lead Sulfide and Copper Indium Diselenide Nanocrystals

CHAPTER 1

INTRODUCTION

Semiconductor nanocrystals have attracted significant interests due to the physical properties that arise as the shape and size (diameter) change for a nanocrystalline particle. These physical properties have been attributed to the quantum confinement effect. As the size of the nanocrystal decreases, the bandgap of the nanocrystal increases, which increases the optical emission from an electron-hole recombination[1]. Current commercial production methods for semiconductor materials include high-cost synthesis techniques that require the use of sophisticated vacuum systems. Examples of these production techniques are Vapor Phase Epitaxy (VPE), Metal Organic Chemical Vapor Deposition (MOCVD), Pulsed Laser Deposition (PLD), and sputtering. The recent advancement in the solution-based synthesis of high quality colloidal nanocrystals provides a potential lower cost alternative.

Quality colloidal nanocrystal synthesis requires three basic components: precursors, organic surfactants and solvents[2]. The synthesis of the nanocrystals can be thought of as a nucleation event, where active atomic species are produced by precursor decomposition which then act as the building blocks for the nanocrystals, followed by a subsequent growth period. Both the nucleation and growth rates were found to be dependent upon factors such as temperature, growth time, and precursor concentration. Production techniques for low-cost synthesis typically utilize batch methods, which have been proven to be effective in producing quality nanocrystals of varying shape, size and composition. Batch methods, however, introduce processing problems due to the difficulty of controlling factors that influence the quality of the nanocrystals. For example, controlling the heat and mass transfer (which are critical in obtaining nanocrystals of uniform shape, size and composition) becomes problematic as the size of the batch reactor is increased. Additionally, batch methods cannot readily adjust to changing reaction chemistries. Continuous flow synthesis methods, on the other hand, allow for the rapid adjustment of the growth temperature, residence time and reaction chemistries. For a continuous flow system the residence time (at nucleation and growth conditions) was also important. In order to separate the nucleation and growth events, injection techniques can be employed to

achieve rapid nucleation of nanocrystals where the final size is dictated by the growth temperature and/or residence time through the growth zone of the reaction system.

Synthesized nanoparticles of lead sulfide (PbS) and copper indium diselenide ($CuInSe_2$) nanoparticles are of particular interest for use in semiconductor, optoelectronics and bio-medical applications. The work presented here focuses on a continuous synthesis method for PbS and $CuInSe_2$ nanocrystals. Experimental parameters (to investigate the resulting size, shape, and composition of synthesized nanocrystals) included injection temperature, residence time, and concentration of organic surfactants. Size tunability was accomplished for both PbS and $CuInSe_2$ nanocrystals that approximated a spherical in shape. Particle sizes less than 10 nm were achieved with compositions reaching approximate stoichiometric ratios for both PbS and $CuInSe_2$.

CHAPTER 2
LITERATURE REVIEW AND BACKGROUND

2.1 Quantum Confinement Effect

The changes to the electronic and optical properties are due to what is called the quantum confinement effect and has drawn attention for the use of size and shape tunable nanocrystals for applications in semiconductors, optics and sensors. The motivation behind synthesizing PbS and $CuInSe_2$ nanoparticles is due to the changes that these materials exhibit when the size of the nanoparticles is less than that of the exciton Bohr radius[1]. The exciton Bohr radius is the measurement of the distance between an excited valence electron with wavelength of energy and the subsequent emission to a lower energy state due to photons as the electron returns to the ground state to recombine with the hole. Energy emitted from the photon is dependent upon the size of the nanocrystal[2, 3]. When at least one dimension of the nanocrystal approaches the exciton Bohr radius, the bandgap for the nanocrystal increases. Also, the bandgap energy increases as the size of the nanocrystal becomes increasingly smaller than the exciton Bohr radius. Quantum confinement depends on the size and composition of the nanocrystal. For PbS nanoparticles the exciton Bohr radius was found to be 18 nm which corresponds to a bandgap of 0.41 eV[4]. For $CuInSe_2$ the value was found to be 10.6 nm for a bandgap of 1.04 eV[5, 6]. Buhro and Colvin[1] also showed that quantum confinement was dependent upon the shape of the nanocrystal. The dimension of confinement follows that a well is confined to one dimension, rods or wires are confined to two dimensions and quantum dots are confined in all three dimensions. With $CuInSe_2$ having a bandgap of 1.04 eV, the material is ideal for a single junction solar cells, which rely upon the utilization of the visible spectrum. Materials with a bulk bandgap value less than or equal to 1.0 eV, like that of PbS, are preferred materials for incorporation into solar cells, light emitting diodes, and bio-imaging sensors in order to utilize the infrared region of solar energy.

2.2 Colloidal Nanocrystals Synthesis

Synthesis of nanocrystals via a solid-liquid interface is called colloidal nanocrystal synthesis. Formation of colloidal nanocrystals requires three components: precursors, surface surfactant and solvents[2]. Nanocrystals in a colloid, at the basic level, are comprised of an inorganic crystal core which is typically stabilized by a layer of organic capping surfactants. These capping surfactants are critical to ensure that the inorganic crystal core is properly encapsulated at the solid-liquid interface, otherwise aggregates will result due to uncontrolled growth and thereby compromising the goal of achieving monodispersed nanocrystals[2, 3]. A properly capped nanocrystal will be suspended in a non-polar solvent such as toluene or chloroform, and characterization techniques such as X-ray diffraction (XRD), transmission electron microscopy (TEM), UV-Vis, photoluminescence (PL) or Raman spectroscopy can be utilized. In order to precipitate the colloids, a polar solvent such as acetone or methanol is needed. Different research has gone into determining the effects of different capping surfactants or ligands. Ligands such as tri-octyl phosphine oxide (TOPO) [7, 8], oleylamine (OLA) [9-13], oleic acid (OA) [14-16], and ethylenediamine[13, 17-20] are a few examples that have been successfully used for synthesis purposes. Non-coordinating solvents such as tri-octylphosphine (TOP) and 1-octadecene are used as solvents, but conflicting reports have been published concerning the role of the non-coordinating solvent in the reaction from precursors to final nanocrystals[5, 11, 14].

2.2.1 General Understanding of Nucleation and Growth Mechanism

The temperature at which the precursors react or decompose is the point for the nucleation. At the nucleation temperature, the precursors become an active molecular species by way of reduction so that the species are electron deficient. These active atomic species are the building blocks for nanocrystal growth. With a

supersaturated active atomic species concentration, nuclei begin to form. Growth of the nanocrystals follows by way of remaining active atomic species suspended in solution being bound onto the nuclei of the nanocrystal. Nucleation and growth conditions are important when synthesizing monodispersed nanocrystals. When slow growth rates are used the general trend is that the resulting crystal size distribution is broad. A phenomenon known as Ostwald ripening is most likely to occur with a slow growth rate due to a low active atomic species concentration. Without an adequate active atomic species concentration, larger particles continue to grow but smaller particles dissolve back into solution and aide in the growth of larger particles[2, 3, 15]. This results in a size distribution that is widely dispersed. Separating the nucleation and growth conditions is favorable.

A typical monodispersed size distribution of nanocrystals is created by first having a supersaturated active atomic species concentration, which creates a sudden nucleation event. As a result, the active atomic species concentration will be low and remaining active atomic species will only be added (during the growth phase) to existing nuclei following the nucleation event. A narrower size distribution of nanocrystals is obtained with a separation of nucleation and growth events.

During the growth of the nanocrystals, the temperature at which growth is undertaken is also vitally important. If the growth temperature is not sufficient, the atoms within the nanocrystals will not be able to rearrange and anneal, and thus a monocrystalline solid will not be able to form[2].

An additional factor that affects growth is the inorganic-organic interface on the nanocrystal. Different ligands provide different surface capping characteristics, as mentioned previously[8, 21-24]. The ligand provides a metal coordinating group that acts as an electron donator. This allows for the ligands to move from the surface of the nanocrystal so that active atomic species can continue adhering to the nuclei of the nanocrystal; however the ligand must also be able to provide enough coverage to prevent aggregation of nanocrystals. Aggregation prevents nanocrystals from growing into a desirable monocrystalline shape such as triangles[22], spheres[7, 8, 14],

rods[19], nanowhiskers[25], or hexagonal rings[24]. Monocrystalline particles are desired due to a lack of defects in the crystal structure which provides for ideal mechanical, optical and electrical physical properties. Not only does the ligand affect the size and shape of the nanocrystal, but functional groups not taking part in the coverage of the nanocrystals are essential in determining the suspension of the nanocrystal[2, 3]. A suspended solution of nanocrystals within a solvent such as toluene is necessary for optical characterization techniques such as UV-Vis or photoluminescence (PL).

Previous work has also been completed on the importance of non-coordinating solvents in synthesizing nanocrystals. However conflicting reports have been published on this topic. One report states that $CuInSe_2$ could not be successfully synthesized without a coordinating solvent[5], while in another report $CuInSe_2$ was successfully synthesized without any coordinating solvent[11]. Published literature shows that the resulting nanocrystals have a wide size distribution with irregular shape and nanocrystals that could not be dispersed in an organic solvent.

2.2.2 Reaction Pathways of $CuInSe_2$ and PbS Colloidal Nanocrystals

For the materials of interest for the current work the following equations show the general reaction pathways for $CuInSe_2$ and PbS nanocrystals:

$$CuCl + InCl_3 + Se \rightarrow Cu_2Se + In_2Se_3 \rightarrow CuInSe_2 \quad (2.1)$$

$$PbO + (tms)_2S \rightarrow PbS \quad (2.2)$$

Note that the above reactions do not include the reaction of the coordinating solvent or other constituents that are used in the actual reaction to produce PbS and $CuInSe_2$ nanocrystals. For the $CuInSe_2$ reaction, the copper and indium chlorides react with oleic acid and elemental selenium reacts with tri-octylphosphine to form TOPSe. Nucleation of copper selenide, indium selenide and $CuInSe_2$ nanocrystals does not occur until a minimum temperature is reached to satisfy formation of active atomic species of Cu^{1+}, In^{3+}, and Se^{2-} that then form the initial nuclei for nanocrystal growth. The synthesis of PbS nanocrystal has similar requirements for reacting the

lead oxide and sulfur complex into precursors, and then a minimum temperature to form the active atomic Species of Pb^{2+} and S^{2-}.

2.2.3 Crystal Structures

Two commonly encountered crystal structures found in synthesizing $CuInSe_2$ nanocrystals are the ordered chalcopyrite[11, 24] (body-centered tetragonal) or disordered sphalerite[11, 24, 26] (face-centered cubic) structures. The difference between the crystal structures for $CuInSe_2$ can be seen in XRD patterns. For sphalerite the major peaks are observed at 26.3° (111), 43.6° (220), and 51.7° (311) whereas for chalcopyrite the major peaks are observed at 26.6° (112), 44.2° (204/220) and 55.4° (116/312). The secondary peaks for chalcopyrite at 17.1° (101) and 35.6° (211) assists with distinguishing between chalcopyrite and sphalerite nanocrystals. Intermediates such as CuSe and In_2Se_3, are possible in the synthesis of $CuInSe_2$, but characterization techniques such as Raman, HRTEM/SAED and SEM help to identify if these intermediates are present.

The crystal structure most commonly used for PbS is the face-centered cubic galena structure. The major XRD peaks are at 25.6° (111), 30.1° (200) , 43.1° (220), 50.9° (311) and 53.4° (222). Other peaks that are indicative of oxides are possible, but the above peaks in tandem with other characterization techniques help to distinguish PbS from any oxide crystal structures.

CaRine Crystallography software was used to build a unit cell model for the crystal structure of PbS, $CuInSe_2$ chalcopyrite[27] and $CuInSe_2$ sphalerite[15, 24]. The crystal structures are found in Figures 2.1 through 2.3, respectively. For the PbS crystal structure the space group was Fm3m (225) with lattice parameters of a=b=c=5.936 Å. Atomic coordinates were: Pb (x=0, y=0, z=0); S (x=1/2, y=1/2, z=1/2). The chalcopyrite $CuInSe_2$ crystal structure has a space group of I-42d (122) with lattice parameters of a=b=5.782 Å, and c=11.619 Å. Atomic coordinates were: Cu (x=0, y=0, z=0); In (x=0, y=0, z=1/2); Se ($x=0.22<a<0.235$, y=1/4, z=1/8). For

the sphalerite crystal structure of $CuInSe_2$ the space group was F-43m (216) with lattice parameters of a=b=c=5.860 Å. Atomic coordinates were: Cu (x=0, y=0, z=0); In (x=0, y=0, z=0); Se (x=1/2, y=1/2, z=1/2).

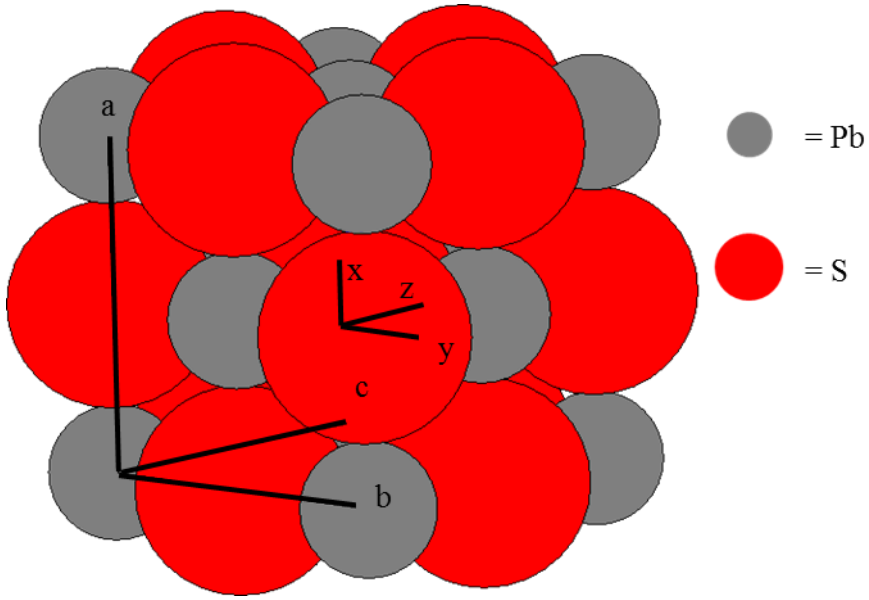

Figure 2.1 PbS face-centered cubic crystal structure.

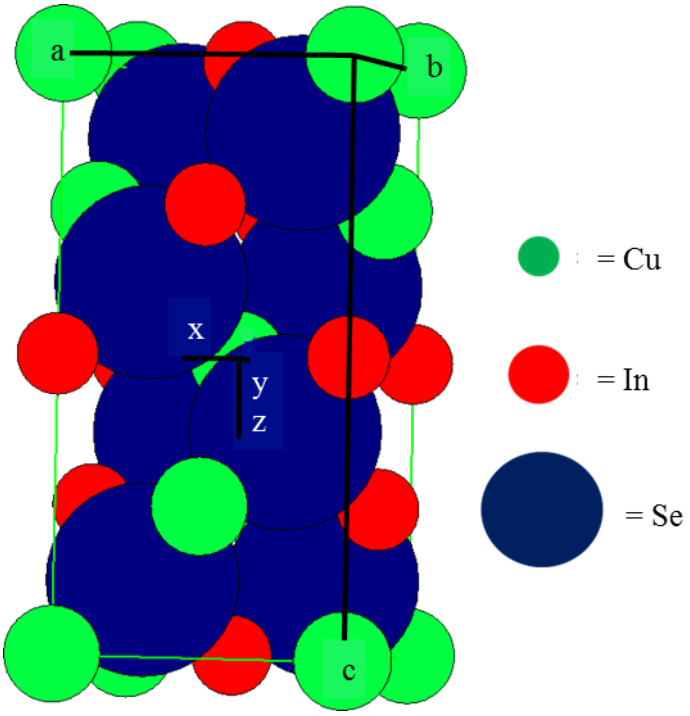

Figure 2.2 Body-centered tetragonal $CuInSe_2$ chalcopyrite.

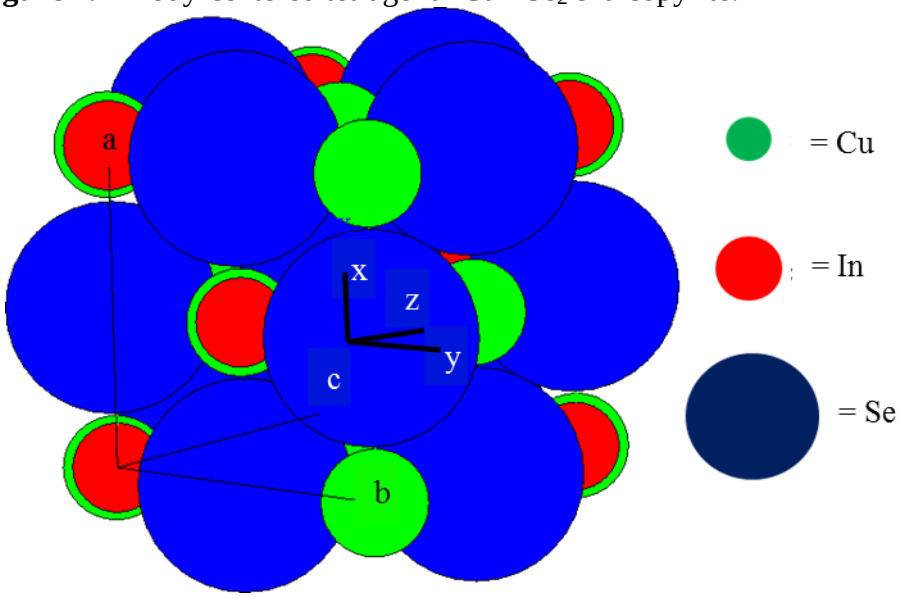

Figure 2.3 Face-centered cubic $CuInSe_2$ sphalerite.

2.2.4 Synthesis Parameters

To obtain nanocrystals that are of a certain size, shape, composition and monodispersed there are several factors that must be considered. Previous sections alluded to the importance of coordinating solvents, nucleation temperature, growth temperature and possibly non-coordinating solvents[2, 3, 5, 11, 28]. Once again the coordinating solvent is essential in providing surface coverage for nuclei to ensure that nanocrystals can grow to be a certain size, shape, and be dispersed in solvent solutions such as toluene or hexane. As a result, the concentration of reactive species in the coordinating complex is important. With a highly concentrated coordination complex, the reactive species will not be able to exchange onto the surface of the nanocrystal. As a result particle size and/or shape will possibly be undesirable. Alternatively, if the concentration of coordination complex is insufficient to provide proper coverage, then the synthesized particles will aggregate.

Adequate nucleation temperatures ensure that there is a sufficiently large concentration of active atomic species in the solution. The active atomic species quickly form nuclei causing the active atomic species concentration to decrease to a point where any remaining active atomic species are only added to existing nuclei. Separation of the nucleation conditions and the growth temperature is essential in controlling the ultimate growth of the nanocrystal as the diffusion of intermediates, the binding energy of coordination complexes to the nanocrystal surface, and the reactive species (and stability of reactive species) all depend on the growth temperature. Too low of a temperature and the active atomic species will not be generated and therefore particle production is not possible, but too high of temperature will lead to uncontrollable particle growth.

Methods for nucleation and growth to synthesize PbS or $CuInSe_2$ have been well studied and the following published works provide methods that have been used for: precursor thermal decomposition[8-10, 13, 15, 16, 24, 28], solvothermal[17-19, 25, 29, 30], microwave-assisted solvothermal[31-33], microwave synthesis[21, 32], microwave-assisted

polyol synthesis[34], pre-mixing of precursors and heating method[5, 6, 11, 12, 22-24]. With these methods, the synthesis was conducted via a batch method. Precursors would be prepared and mixed or injected together at prescribed nucleation temperatures, and the subsequent growth would be controlled by changing the temperature input to the system. With the synthesis presented here, the preparation method that was chosen was a continuous flow system in conjunction with precursor thermal decomposition. Precursor thermal decomposition is needed in order to achieve the sudden supersaturation of active atomic species and form the desired nuclei in a quick manner. As a result of this processing change another important factor to consider is the residence time that the reactants and products reside within a certain segment of the reaction system. Residence time affects the time in which precursors have to form active atomic species to initiate nucleation, and also affects the time in which particles can continue to grow. Ultimately the residence time is used to control the growth of the particles as well, where the residence time is changed by changing the pump flowrates or by changing the reactor dimensions, such as the diameter or length.

CHAPTER 3
MATERIALS AND RESEARCH METHODS

3.1 Synthesis Methods

The PbS (binary) and $CuInSe_2$ (ternary) compounds were selected for proof of concept purposes in a continuous flow synthesis system to obtain particles that are monocrystalline with the desired, shape, stoichiometric composition and crystal structures (cubic for PbS and tetragonal-chalcopyrite for $CuInSe_2$)[23, 35]. Continuous flow synthesis was also selected for comparison purposes to batch synthesis methods that included: precursor thermal decomposition[8-10, 13-16, 24, 28, 36-38], solvothermal[17-19, 25, 29, 30], microwave-assisted solvothermal[31-33], microwave synthesis[21, 32], microwave-assisted polyol synthesis[34], pre-mixing of precursors and heating method[5, 6, 11, 12, 22-24], chemical bath deposition[36], epitaxial synthesis[37, 38], and other synthesis methods[37-39]. Experimental parameters selected for determining the effect on nanocrystal quality included: injection and growth temperature, residence time and concentration of the coordinating solvent, oleic acid. The above parameters ranged in values that were dependent on either synthesizing PbS or $CuInSe_2$. A more in depth explanation and layout of the PbS or $CuInSe_2$ experiments can be found in the experimental tables found in each respective section in Chapter 4.

3.2 Materials

Copper (I) chloride (ACS 90+%, Alfa), indium (III) chloride anhydrous (99.99%, metal basis, Alfa), and selenium powder, -325 mesh (99.5%, metal basis, Alfa) were purchased and used without further purification. Trioctylphosphine (TOP) (technical grade, 90%, Aldrich), and oleic acid (OA) (technical grade, 90 %, Aldrich) were purged with nitrogen gas to remove any oxygen that may have been present were used for $CuInSe_2$ synthesis experiments.

Lead oxide (II) oxide (PbO) (99.999% metal basis, Aldrich), hexamethyldisilathiane ($(tms)_2S$) (synthesis grade, Aldrich), 1-octadecene (1-ODE) (technical grade, 90%, Aldrich), and oleic Acid (OA) (technical grade, 90%, Aldrich) were used for PbS synthesis runs.

3.3 Precursors Preparation and Synthesis

The recipe for $CuInSe_2$ synthesis was adopted from Jin[15]. For PbS synthesis, the recipe from Hines and Scholes[14] was adopted.

3.3.1 TOPSe Precursor

The 1.4 mmol/mL TOPSe precursor was made with selenium powder (1.33 g) and TOP (12 mL). The TOPSe mixture was shaken vigorously, which resulted in an exothermic reaction and the solution went from black to clear. Any residual selenium powder was dissolved by stirring the TOPSe mixture at 90°C for 30 minutes to give a completely clear solution of TOPSe.

3.3.2 Precursor of Cu+In with OA/TOP

The volumetric ratio of OA to TOP was 4:1, so that a 30 mL solution contained 24 mL OA and 6 mL TOP. A mixture of 0.11 mmol/mL of CuCl (0.33 g CuCl per 30 mL OA+TOP) and 0.34 mmol/mL of InCl3 (0.33 g $InCl_3$ per 30 mL OA+TOP) was prepared as the Cu/In precursor. The mixture was stirred at a temperature of about 90°C for two hours until dissolved in TOP and OA and the color turned to a light yellow (lemonade-like) color. An important observation was to keep the non-dissolved metal chlorides suspended in the solution, as any precipitated metal chlorides would turn a dark brown color. This was due to a non-uniform temperature difference from the bottom of the beaker and the solution.

Subsequent synthesis using this brown solution would not yield $CuInSe_2$ particles. The reactant from the undesired reaction of Cu during precursor preparation was not investigated beyond experimental observation.

3.3.3 $CuInSe_2$ Synthesis

The Cu/In precursor was pumped into one end of a T-mixer at a flowrate of 0.3 mL/min while the TOPSe precursor was pumped at a flowrate of 0.1 mL/min into the other leg of the T-mixer. The reaction time was controlled by varying the length of 1/16" inner diameter Viton tubing immersed in a hot silicone oil bath where temperature was held at the desired growth temperature, between 190°C and 250°C. The residence time within the growth zone was determined by the desired nanocrystal growth time and fixed by the total volumetric flowrate.

3.3.4 Lead Oleate Precursor

A typical precursor recipe would include 0.1 mmol/mL of PbO (0.45 g PbO dissolved in 20 mL OA/ODE). The PbO was dissolved in OA/ODE at 150°C for one hour under constant stirring conditions. The ratio of OA to ODE affected the size of the resulting nanocrystals. Larger nanocrystals were obtained from a lead oleate precursor solution containing only OA, whereas much smaller nanocrystals were obtained with a ratio of 1.5 mL OA to 18.5 mL ODE in the lead oleate precursor.

3.3.5 Sulfur Precursor

For the sulfur precursor a typical precursor recipe would follow the 2:1 molar ratio of Pb to S, thus the sulfur precursor included 210 µL $(tms)_2S$ per 10 mL ODE. No heat treatment was needed to further dissolve $(tms)_2S$ in ODE.

3.3.6 PbS Synthesis

The $(tms)_2S$ /ODE precursor was injected into the lead oleate precursor at temperatures varying from room temperature to approximately 90°C. The reaction time was controlled by the length of 1/16" inner diameter Viton tubing immersed in a hot silicone oil bath where temperature was held at a desired growth temperature, between 90°C to 150°C. The residence time within the growth zone was determined by the desired nanocrystal growth time and fixed by the total volumetric flowrate or tubing length.

3.3.7 Experimental Setup

The experimental setup is shown in Figure 3.1. The equipment used for pumping was either: Lab Alliance Series I pumps with stainless steel pump heads, KD Scientific syringe pumps with a 30 mL syringe and 20 gauge tip, or Ismatec-IDEX Corporation Reglo peristaltic pumps (model numbers: ISM834C and ISM 5971) with 1/16" inner diameter Tygon® tubing. The stainless steel tubing that was used to pre-heat the lead oleate or Cu/In precursor was replaced with Viton tubing due to chemical interactions with the stainless steel alloys, and the reason why the stainless steel Lab Alliance pumps were removed from synthesis runs as well. Due to needing elevated temperatures (250°C in the case of $CuInSe_2$ synthesis) for nucleation and growth a stainless steel T-mixer was used followed by Viton tubing, both of which could withstand the elevated temperatures. The length of tubing used for preheating and for the growth zone was dependent upon the desired residence time through each section. The experimental setup in Figure 3.1 is for general purposes and setup to show (1) the pumps used to pump the (2) precursors which are then pumped to (4) the concentric T-mixer followed by flow through (3) the Viton tubing that is submerged in silicone oil on top of a temperature controller.

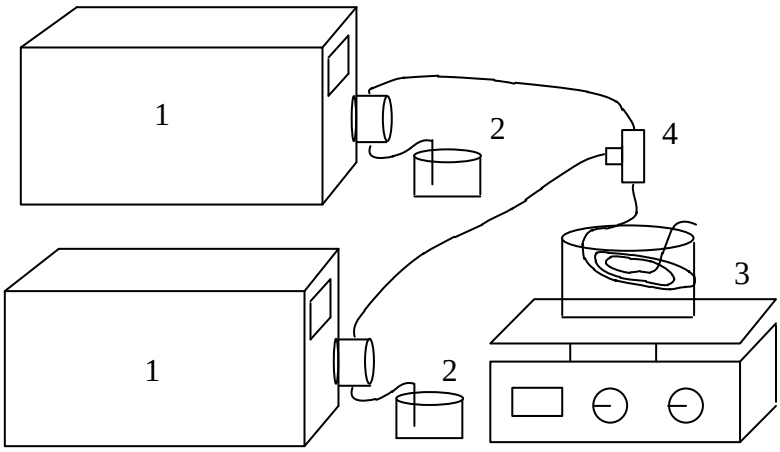

Figure 3.1 General experimental setup

3.3.8 Post-Processing

Sample collection was accomplished in a glass vial that contained 7 mL of Methanol (anhydrous, Alfa) to precipitate the synthesized particles. Sample collection was done for three to five minute time intervals. Precipitated particles were collected by centrifugation of the sample vials at 5,000 RPM for a time of 10 minutes to one hour depending on how well the particles would precipitate out of solution. The supernatants were discarded and the remaining precipitates were suspended in toluene (99.9% HPLC grade, Aldrich).

3.4 Characterization of Materials

3.4.1 Transmission Electron Microscopy (TEM)

Low resolution images were collected using a Philips CM-12 TEM, operating at 80KV, and high resolution images (HRTEM) were taken using a FEI Titan FEG-TEM operating at 200KV. Samples were drop-cast using the toluene suspension onto either a carbon coated 300-mesh copper grid or carbon coated 300-mesh gold grid. Nanoparticle sizes were determined by using Image J - National Institutes of

Health developed software. A wide size distribution of nanocrystals results in a COV value that approaches one which is undesirable. From the HRTEM images within Image J, Fast Fourier Transform (FFT) images were used to obtain diffraction patterns to measure lattice spacings of individual nanoparticles. From low resolution images, Scanning Area Electron Diffraction (SAED) was also used to obtain diffraction patterns of bulk crystals.

3.4.2 X-Ray Diffraction (XRD)

The phase and the crystallographic structure of synthesized particles were characterized with a Bruker-AXS D8 Discover instrument using Kα radiation with a wavelength of 1.54 Å. Material was drop-cast from the toluene suspension onto a glass slide and placed on a transparent puck to prevent any responses from the aluminum stage. Diffraction data collection was conducted using a 5°/min scan rate (0.05° increments). Background interference was removed by use of the Bruker-AXS EVA software program with the final data exported as text files for later plotting in Microsoft® Excel. Files used for reference were JCPDS 40-1487 for chalcopyrite $CuInSe_2$, JCPDS 75-2433 for In_2Se_3, JCPDS 80-2272 for CuSe, JCPDS 5-592 for PbS, and JCPDS 78-1665 for PbO. The Scherrer Equation was used to determine bulk crystallite diameter of a sample. The following is a general form of the Scherrer Equation:

$$d = \frac{K\lambda}{B\cos\theta_B}$$

d = crystallite diameter (nm)

K = crystallite shape constant (using 0.9 for spherical shape)

λ = x-ray wavelength (0.154 nm)

B = Full-width at half max at Bragg angle of interest

θ_B = Bragg Angle (angle of interest)

3.4.3 Energy Dispersive Spectroscopy (EDS)

The sample composition was determined using a FEI Quanta 600 FEG SEM (Scanning Electron Microscope). All analysis operations were done in high vacuum with the working distance (WD), voltage and spot size all dependent upon desired image results. Samples were prepared by drop-casting the toluene suspension onto a silicon wafer and dried under N_2 gas. Samples were characterized using multiple locations on a sample and the compositions were determined using the on-board EDAX Genesis Apex EDS system.

3.4.4 UV-Vis and Photoluminescence (PL)

A Perkin Elmer Lambda 9 UV-Vis-NIR spectrophotometer was used to obtain absorbance data. Samples were prepared by diluting samples in toluene after getting a baseline reading for the spectrometer. A cuvette of pure toluene was used in parallel during absorbance runs as a reference for the samples. After obtaining UV-Vis results, PL was completed on an Edinburgh FLS 900 fluorimeter with an Osram XBO 450 OFR Xenon short arc 450W bulb. Filters were selected depending on the material system and expected wavelength for emission. For a direct bandgap material the following equation was used to determine the bandgap at zero absorbance.

$$(ah\nu)^2 = h\nu - E_g \; ; \quad ; \quad E_g = \frac{h\nu}{\lambda}$$

a = absorbance coefficient (μm^{-2})

$(ah\nu)^2$ = absorbance coefficient ($\mu m^{-1} eV)^2$

E_g = Band gap energy (eV)

$h\nu$ = photon energy = 1.24 μm-eV

λ = wavelength of light (nm)

3.4.5 Raman Spectroscopy

Raman results were obtained using a Horiba-Jobin Yvon HR800 Raman Spectrometer. Spectral results were collected using the following conditions: 532 nm laser at 50% power, hole size of 200 µm, a D2 filter was used from command input into the computer program, spectrometer wavelength of 532 nm, grating of 1,200 µm, objective of 100x, accumulation of 5 seconds and 30 acquisitions.

CHAPTER 4
ANALYSIS AND DISCUSSION OF RESULTS

4.1 $CuInSe_2$ Synthesis

The work completed on $CuInSe_2$ is an extension of the work previously discussed by Jin[15]. Synthesis of ternary $CuInSe_2$ nanocrystals was chosen in order to show an extended proof of concept using a continuous flow system rather than batch methods. The $CuInSe_2$ synthesis investigated the effect of injection temperature, residence time, and concentration of organic surfactants on the quality of nanocrystal size, shape and composition

Prior to discussing the results from the effects of injection temperature, initial synthesis revealed information about the minimum temperature for a nucleation event to occur, in order to obtain $CuInSe_2$ nanocrystals, not previously mentioned[15] with the recipe used. The approximate nucleation temperature for the reaction system and recipe outlined in Chapter 3 was found to be around 190°C. For explaining $CuInSe_2$ results, Table 4.1 includes the experimental parameters and further discussion of the results will be referenced as "run x" for the presented figures or tables. The column labeled "other" represents changes in coordinating solvent concentration, pumping technique or system setup. Unless otherwise noted, the concentrations of the precursors follow those given in sections 3.2.1 and 3.2.2.

Results of run 1 can be seen in Figure 4.1. The general trend from Figure 4.1, excluding the 20 minute residence time, shows that intermediates become less pronounced as residence time increases. These results suggest that synthesis of $CuInSe_2$ was accomplished, as the primary peaks at 2θ values of 26.6° (112), 44.2° (204/220) and 55.4° (116/312) were present. The phase of $CuInSe_2$ cannot be determined due to the lack of secondary peaks at 17.1° (101) and 35.6° (211), which are indicative of the chalcopyrite crystalline phase.

Table 4.1: $CuInSe_2$ synthesis runs

Run #	Injection Temperature (°C)	Growth Temperature (°C)	Residence Time (min)	Other	Figure (F) or Table (T) #'s
Run 1	20	195	6, 8, 10, 20	Lab Alliance pumps, Stainless steel tubing for Cu/in precursor, T-mixer	F 4.1
Run 2	20	195	8, 10, 20	Peristaltic Pumps, Viton tubing	F 4.2
Run 3	~90	200, 215	8, 10, 20	KD Scientific Syringe pump, Stainless steel tubing for Cu/In precursor	F 4.3
Run 4	~90	195, 215	8, 10	KD Scientific Syringe Pump, Viton tubing, one sample of 1:4 OA:TOP, one sample with sonication used in wash method	F 4.4-4.6
Run 5	~140	250	4, 6, 8	Peristaltic Pumps, Viton tubing, T-mixer	F 4.7-4.11 T 4.2
Run 6	~230	250	6, 8	T-Mixer moved to silicone oil bath surface	F 4.12-4.18
Run 7	~230	250	6, 8	T-Mixer moved to silicone oil bath surface and 1:4 OA to TOP ratio by volume in Cu/In precursor (1.5 mL OA and 18.5 mL TOP)	F 4.19-4.20

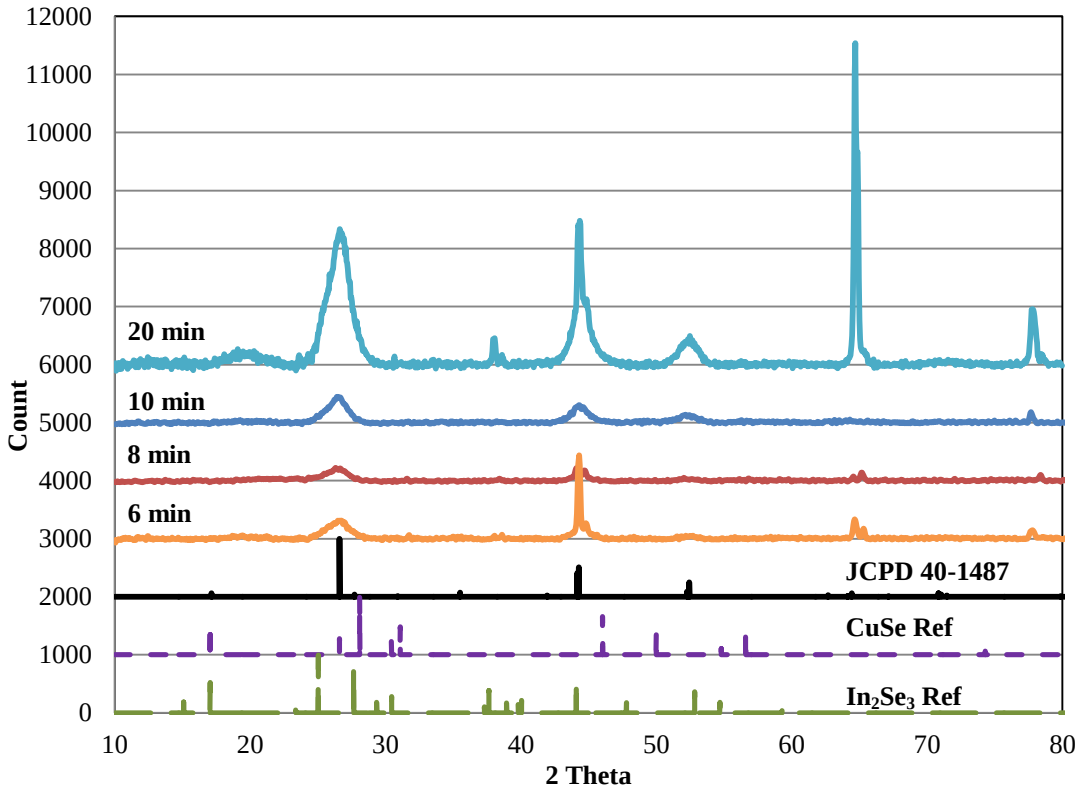

Figure 4.1 XRD analysis of run 1 indicating $CuInSe_2$ characteristic peaks with intermediates present.

The counts for all samples approximately had the same baseline value, for figure clarity when comparing the different samples in Figures 4.1, 4.2, 4.3, 4.9, 4.13, 4.20, and 4.23 an arbitrary offset was applied to these baselines in order separate the counts for each run. Problems with intermediates can be seen with the XRD results shown in Figure 4.1. The peak at 79° was the most notable since the peak cannot be identified with $Cu_xIn_ySe_z$, Cu_xSe_z, In_ySe_z, or oxide intermediates. Additionally, the intense and narrow peaks at 44° for the 6 minute residence time and the 65° peak for the 20 minute residence time indicate intermediates were present. Another observation from this synthesis was that the precipitate was dark brown at 6 minutes and darkened to a black color as the residence time increased. This was an indication of copper selenide and indium selenide intermediates[5, 11, 12, 25, 34]. This matches well with the findings from Kar and co-workers[12] that stated if the pre-

cursors are mixed below the nucleation temperature that CuSe would form at 130°C, followed by nucleation of InSe and $CuInSe_2$ particles at 195°C. From run 1 the growth temperature of the silicone oil bath was approximately 195°C, meaning that there were In_xSe_y intermediates formed to produce $CuInSe_2$ but not in sufficient amounts to fully convert Cu_xSe_y intermediates to $CuInSe_2$ particles. As a result, lower residence times and lower temperatures were not sufficient in terms of reaction conditions to convert the pre-cursors fully from intermediates to the final desired $CuInSe_2$ chalcopyrite phase[11]. This was supported by the increasing intensity of intermediate peaks at 30.1° and 31.7° which closely resembled the In_xSe_y intermediate. Experimental observation indicated that as residence time increased particle production changed from faint, hard-to-see particles at a 6 minute residence time to very distinctive and large aggregates of particles at a 20 minute residence time.

To build upon run 1, run 2 investigated changes in tubing from stainless steel to polymer and run 3 was done to explore the increased growth temperatures of 200°C and 215°C. With run 2, the absence of the peak at 78° in Figure 4.2 provided an insight that the metal halides present in the Cu/In pre-cursor were reacting with the stainless steel pump head of the Lab Alliance pump and the stainless steel tubing used in run 1. Peristaltic pumps that utilized Tygon® and Viton® tubing were used for the run 2. The peak at 78° was once again present in run 3 as seen in Figure 4.3, where a single syringe pump was used, however the stainless steel tubing from run 1 was once again used. With the results of runs 1 through 3 and comparing to possible reaction pathways[11] when using a coordinating solvent, the precursors reacted to create chlorinated intermediates that etched the stainless steel pump heads and tubing.

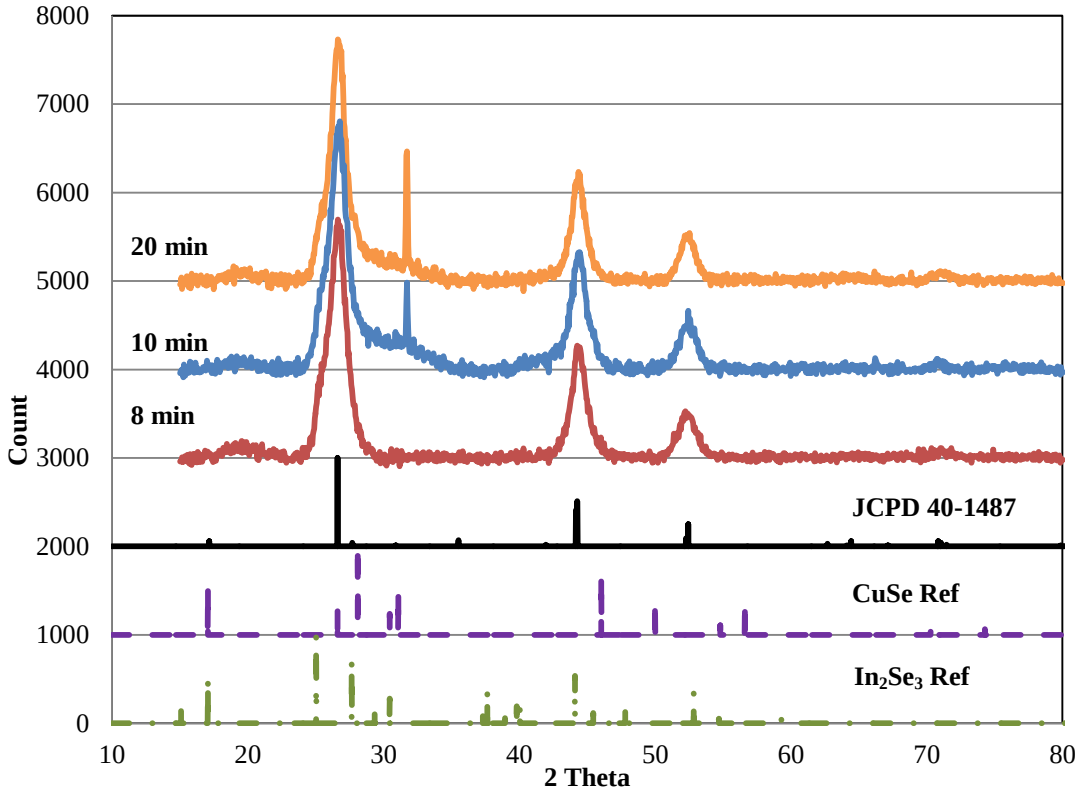

Figure 4.2 XRD of run 2 indicating $CuInSe_2$ characteristic peaks.

The shorter residence times and lower reaction temperature used for run 2 are not sufficient in terms of reaction conditions to convert the precursors to intermediates and finally to the $CuInSe_2$ chalcopyrite phase[11] as was found with run 1. The sample from an 8 minute residence time synthesis did not provide a distinctive peak at 70.1° (316) but was present for the sample from 10 minute residence time and again, with an increased intensity, at a 20 minute residence time synthesis. The major peaks at 2θ values of 26.6° (112), 44.2° (204/220) and 55.4° (116/312) for $CuInSe_2$ were present; furthermore the intensity increases with increasing residence time indicating a growing bulk particle size. The peak at 31.6° was intensive and sharp indicating an intermediate that became more pronounced as the residence time increased. A possible explanation can be due to intermediate nanocrystals, meaning that at larger residence times there was an excess of Cu_xSe_y or In_xSe_y nanocrystals as a result of increased conversion of precursors to intermediates.

Also, the large shoulder directly following the $CuInSe_2$ peak at 26.6° (112), can be attributed to Cu_xSe_y or In_xSe_y intermediates[11, 24]. Additional characterizations to analytically determine if these intermediates (CuSe, InSe, In_2Se_3 or analogous indium/copper selenide structures) were present were not completed in this work.

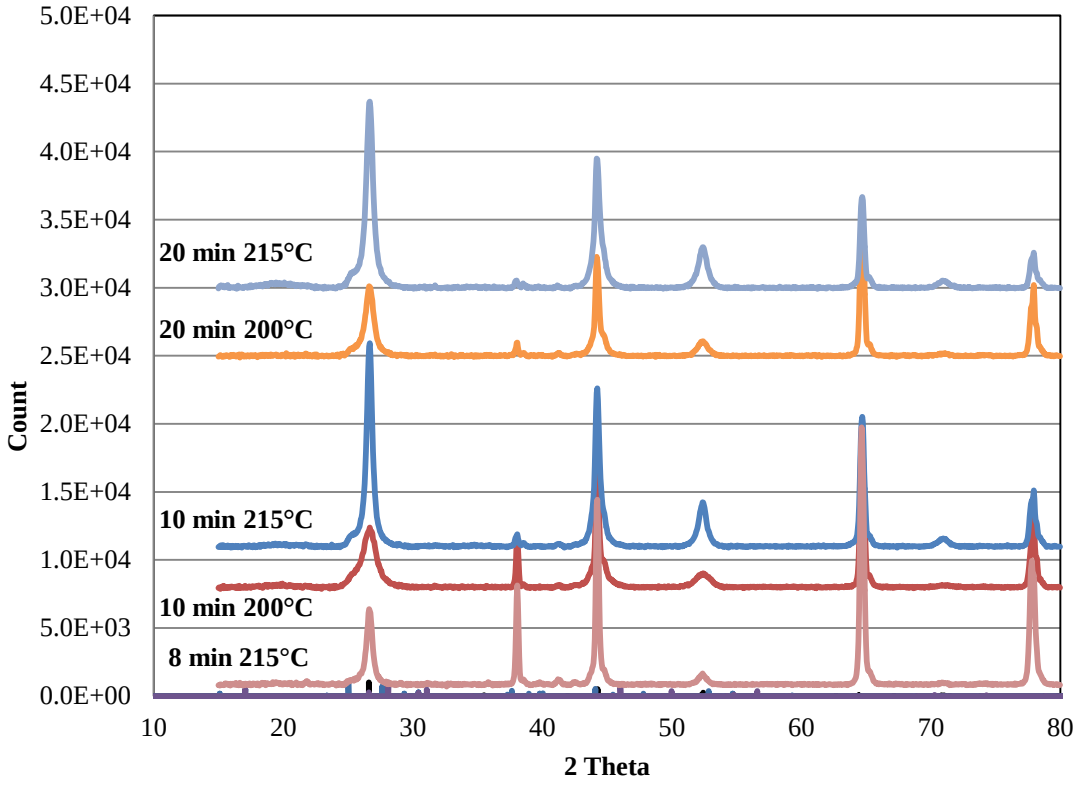

Figure 4.3 XRD of run 3 showing reduced intensity at increased growth temperature for $CuInSe_2$.

When looking at the results for run 3, the peaks become increasingly broad and less pronounced in terms of peak intensity as the residence time increases, as a result of the diffracting particles being smaller due to increased conversion of copper selenide and indium selenide intermediates forming $CuInSe_2$ nanocrystals. Although not measured or investigated here, the thought is that copper selenide forms larger plate-like crystals and the indium selenide forms large spherical crystals, after which smaller $CuInSe_2$ nanocrystals are formed[11]. From the Scherrer Equation, run 3 showed a bulk crystallite size of approximately 40 nm for the 8 minute-215°C

sample and about 20 nm for the 20 minute-215°C sample. Results of runs 1 through 3 showed that by injecting below the nucleation temperature, the precursors would react to form Cu_xSe_y first, followed by In_xSe_y and finally forming $CuInSe_2$. Also, as the temperature for growth increases from 200°C to 215°C the trend shows that the intermediate seen at 38.1° decreased and can be most closely assigned to Cu_xSe_y. This fits well with the results from Kar and co-workers[11], where they found that as temperature for growth increased the CuSe and InSe intermediates were replaced by $CuInSe_2$ nanocrystals. XRD patterns from run 1 through run 3 indicate a sharpening of the peaks, especially the 26.6° (112), and 44.2° (204/220) peaks, for increased growth temperature. The sharpening of the peaks suggests that the purity of the nanocrystals being synthesized was increasing, which is desired.

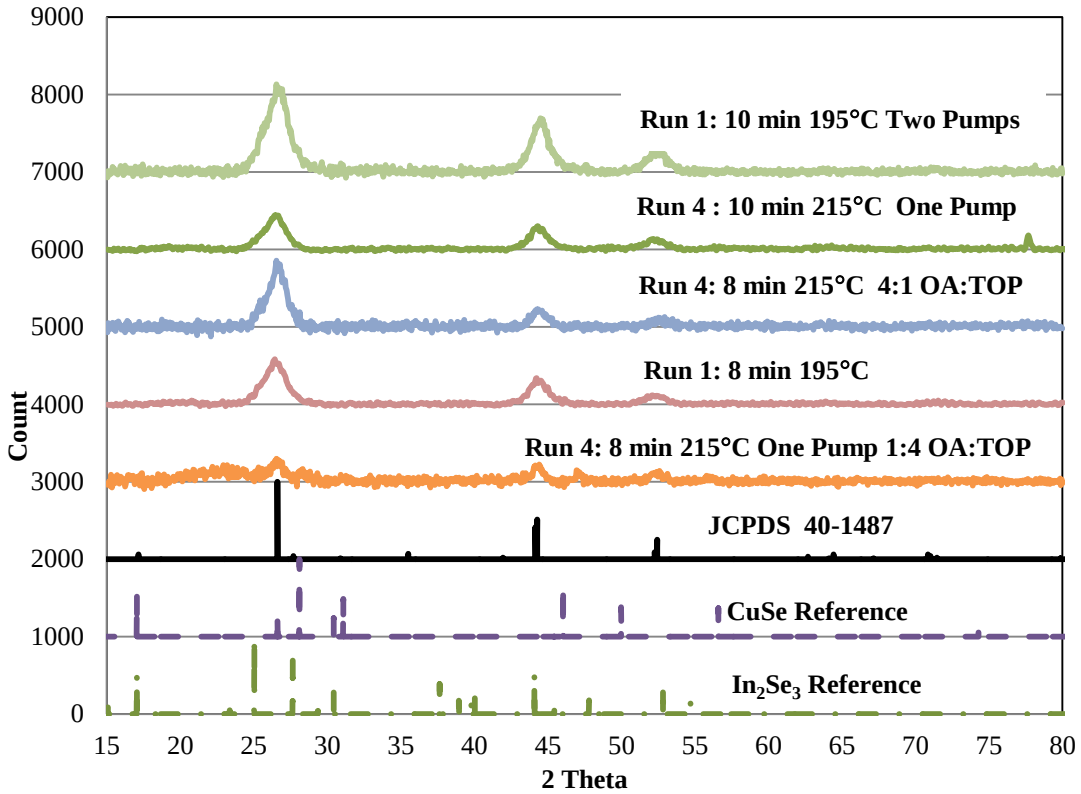

Figure 4.4 XRD of run 4 indicating broad $CuInSe_2$ characteristic peaks and lack of intermediate peaks.

Results from run 4 provided confirmation of results found in run 3 that at an increased growth temperature from runs 1 and 2, 195°C to 215°C, the intermediates of copper selenide and indium selenide were increasingly converted to $CuInSe_2$[11]. From Figures 4.4 and 4.3 peaks sharpening shows that the particles are becoming larger in size for $CuInSe_2$ when compared to run 1. Further comparison of runs 3 and 4, show that as residence time increases the peaks are also becoming sharpened. Both residence time and growth temperature are important for being able to control the size of nanocrystals being synthesized.

TEM imaging of the 8 minute residence and 215°C growth temperature trial showed that for run 4 the particles were highly agglomerated and that the agglomeration lacked distinct individual particles in Figures 4.5 and 4.6. The agglomerates were all several hundred nanometers in size and could possibly indicate that the washing method was not sufficient. From the observations from run 4 a more rigorous wash method was implemented for run 5.

Changing the ratio of OA:TOP from 4:1 to 1:4 for run 4 resulted in $CuInSe_2$ intermediate crystallite formation. The shoulders in Figure 4.4 at 28.4° and 47.1° fit that of CuSe. This theory is supported by the experimental observation that the color of the particles and supernatant liquid was a dark brown not the black color representative of the $CuInSe_2$ chalcopyrite crystal phase and that the additional peaks are not representative of the sphalerite phase of $CuInSe_2$ and as a consequence CuSe was the result of this synthesis recipe[6, 11].

The one-pump results for run 3 (Figure 4.3) and run 4 (Figure 4.4) showed that premixing the pre-cursors at room temperature and then bringing the mixture to growth temperature conditions was comparable to using the two-pump system from runs 1 and 2. All four runs mixed pre-cursors at temperatures well below the nucleation temperature of 190°C, followed by gradually heating the mixed pre-cursors to the desired growth temperature for each respective run.

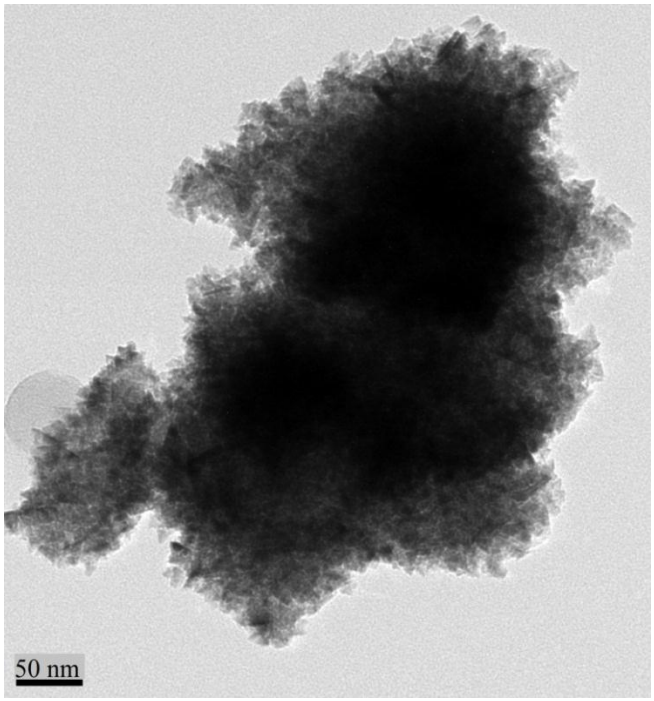

Figure 4.5 Large agglomeration of $CuInSe_2$ nanocrystals grown at 215°C and 8 minute residence time.

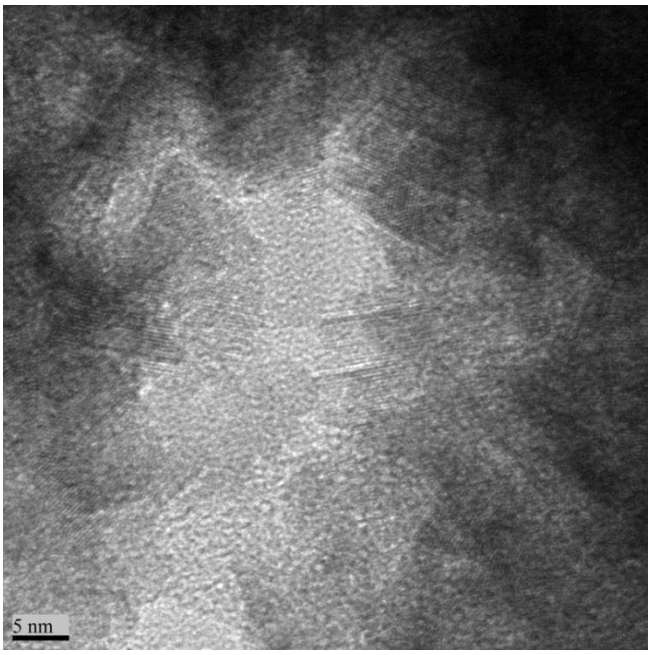

Figure 4.6 HRTEM with overlapping $CuInSe_2$ nanocrystals grown at 215°C and 8 minute residence time.

The two pump system was required for the run 5 synthesis. The motivation was to inject the Cu/In precursors at an elevated temperature, which was not possible using the single pump system used for runs 3 and 4. This synthesis method also included a more rigorous washing step to investigate how much washing plays a role in dispersing particles due to large agglomeration problems found in run 4:

1. Particle precipitation in methanol
2. Centrifuge at 5,000 RPM followed by decanting supernatant
3. Suspend particles in toluene with sonication for 10 minutes
4. Repeat steps 1 through 3 two more times

The results of from run 5 with sonication are shown in Figures 4.7 and 4.8 for a growth temperature of 250° and residence time of 8 minutes. TEM imaging indicated that the more rigorous washing method using sonication assisted in dispersing the $CuInSe_2$ nanoparticles. Agglomeration was still an issue; however individual ~5 nm particles can be seen in Figures 4.7 and 4.8, which cannot be measured or readily observed in the non-sonicated run 4 sample shown in Figures 4.5 and 4.6.

XRD analysis results of the nanoparticles synthesized during run 5 are shown in Figure 4.9. The results are characteristic of the $CuInSe_2$ crystal structure and closely match the results from previous synthesis runs. Several observations were noted from the run 5 XRD results. First was the validation of the need for a more rigorous post-processing washing method. This need was exemplified by the results that the average crystallite size, as determined by the Scherrer Equation, was 27 nm for the unwashed particles and 5 nm for the washed sample. The 5 nm nanocrystal size from the Scherrer Equation in Figure 4.9 was approximately the same nanocrystal size that was found with the TEM images in Figure 4.7 and 4.8. Another observation from Figure 4.9 was that the major characteristic peaks for $CuInSe_2$ became more intense and sharpened in width as the growth temperature increased from 195°C to 250°C, matching the results found in literature[11].

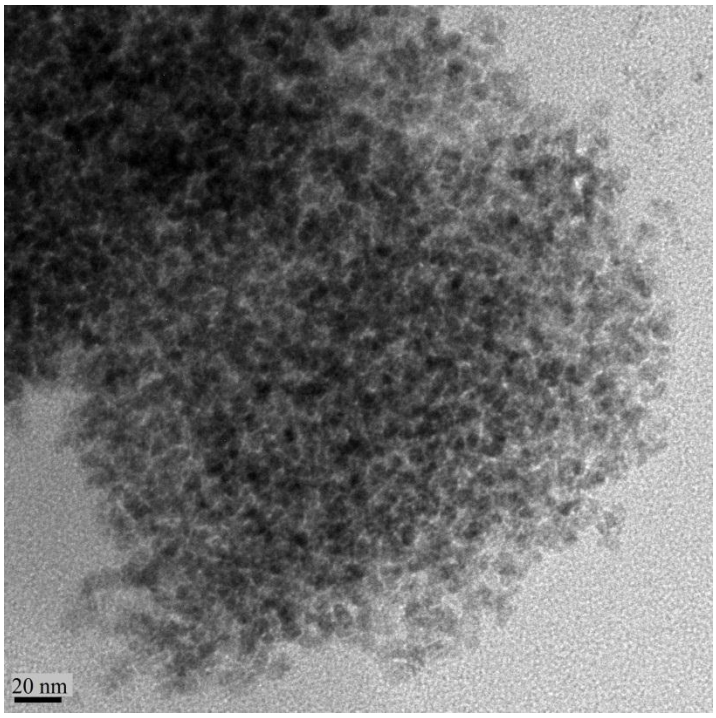

Figure 4.7 Agglomerated $CuInSe_2$ nanocrystals with distinct single crystals from run 5.

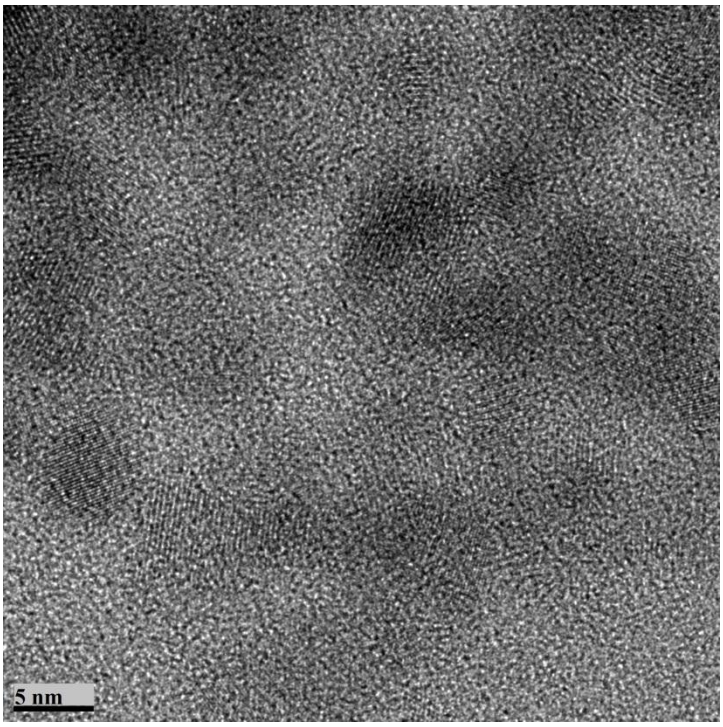

Figure 4.8 HRTEM of agglomerated of $CuInSe_2$ nanocrystals from run 5.

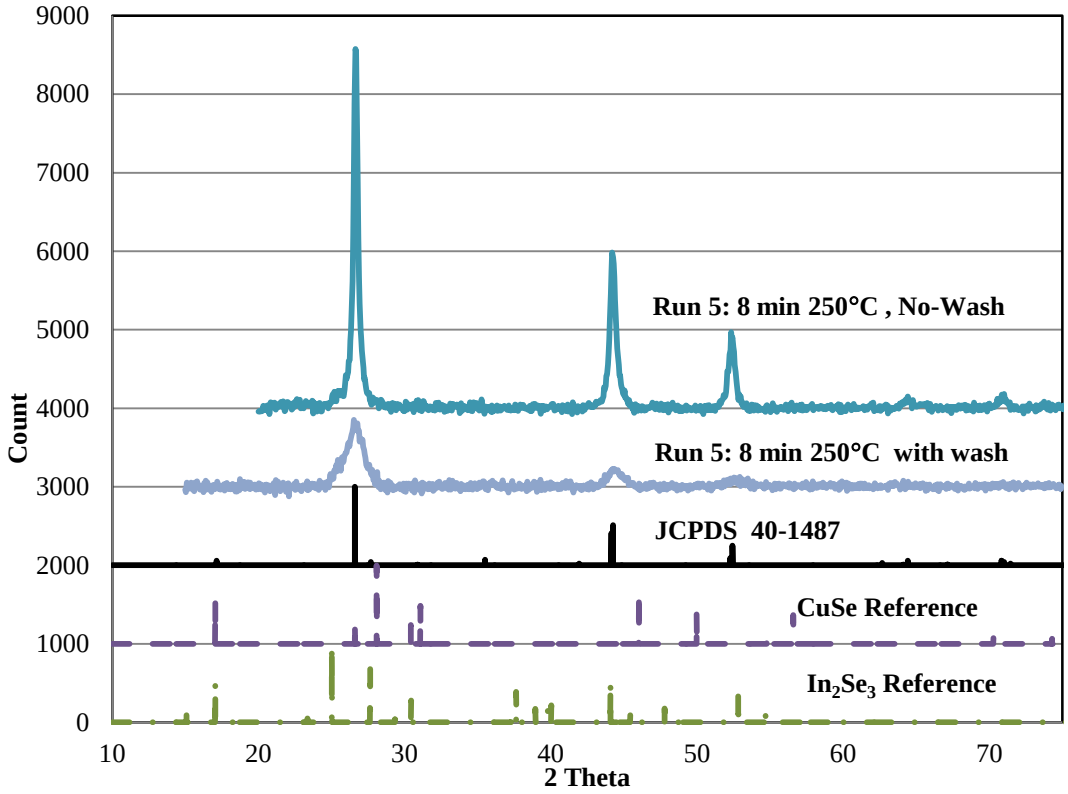

Figure 4.9 XRD showing characteristic peaks for $CuInSe_2$ for run 5.

The importance of further post-processing methods can be seen in the differences between Figure 4.10 and Figure 4.11 for the 8 minute residence time in run 5. In Figure 4.10, single nanocrystals are agglomerated together but with the appearance of reaction byproducts that was deposited within the agglomerated structure. This was assumed because in Figure 4.11 much of the interparticle sheen film that can be seen in Figure 4.10 has been removed. With Figure 4.11 the particles appear to be more agglomerated compared to Figure 4.10. In Figure 4.10, the particles appear to be larger and individual particles can be seen within the agglomerate, whereas in Figure 4.11 the particles have more of a finer cauliflower look.

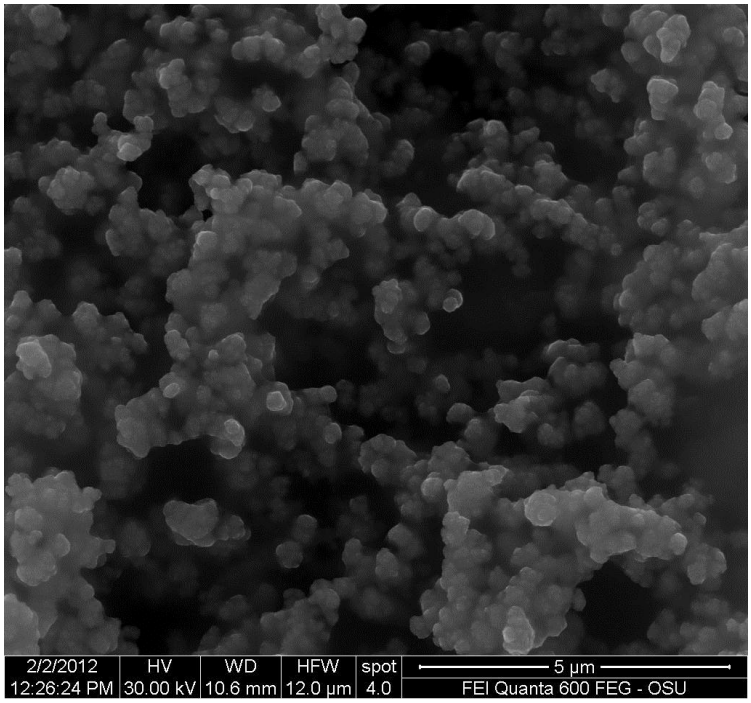

Figure 4.10 As-synthesized $CuInSe_2$ nanocrystals from run 5.

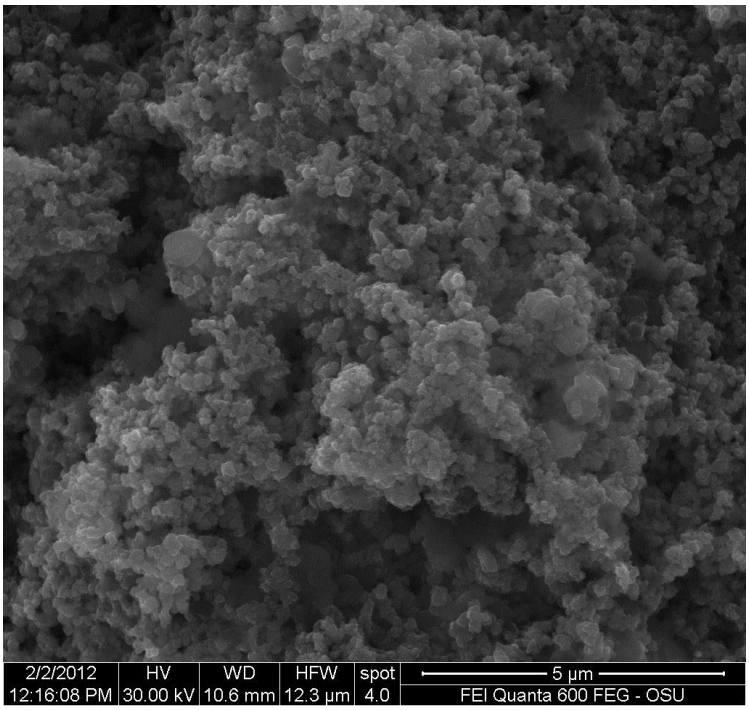

Figure 4.11 $CuInSe_2$ nanocrystals using a triple-wash and sonication method from run 5.

EDX was also completed on the samples from run 5 to determine the surface composition of the $CuInSe_2$ nanocrystals. As can be seen in Table 4.2, as residence time increases during run 5 the indium selenide intermediates increase on the surface of the nanocrystals. This was found to be in agreement with literature[11] as well. At the 4 minute residence time, the presence of CuSe intermediates is apparent on the surface of the $CuInSe_2$ nanocrystals.

Table 4.2 EDX results indicating increased In_2Se_3 crystal dissolution and formation into the $Cu_xIn_ySe_z$ crystal structure.

Reaction Conditions	Element	At %	Cu:In:Se
250°C 4 minute residence time	Cu	25.49	1.00: 0.7: 2.19
	Se	55.94	
	In	18.57	
	Total	100.00	
250°C 6 minute residence time	Cu	24.38	1.00:0.85:2.25
	Se	54.82	
	In	20.80	
	Total	100.00	
250°C 8 minute residence time	Cu	19.20	1.00:1.19:3.00
	Se	57.81	
	In	22.99	
	Total	100.00	

The results for run 6, with the injection and growth temperature at 250°C, demonstrated sharpened peaks that corroborate well with previous results[11]. From the Scherrer Equation, the average crystallite size was approximately 9 nm for the 8 minute residence time results for run 6 shown in Figure 4.12. As a comparison the diameter was found to be about 5 nm for the 8 minute residence time for run 5 shown in Figure 4.9, which was at a 140°C injection temperature and a 250°C growth

temperature. Rather than injecting below the nucleation temperature of 190°C and using the growth zone to create both the nucleation and growth of nanocrystals like that in run 5, a nucleation zone at 250°C appears to result in increased particles growth for equivalent residence times. Low concentrations of In_xSe_y intermediates are possibly visible with the left-shoulder at 25° for the 6 minute residence time in Figure 4.12 for run 6, but this shoulder was not apparent with the 8 minute residence time.

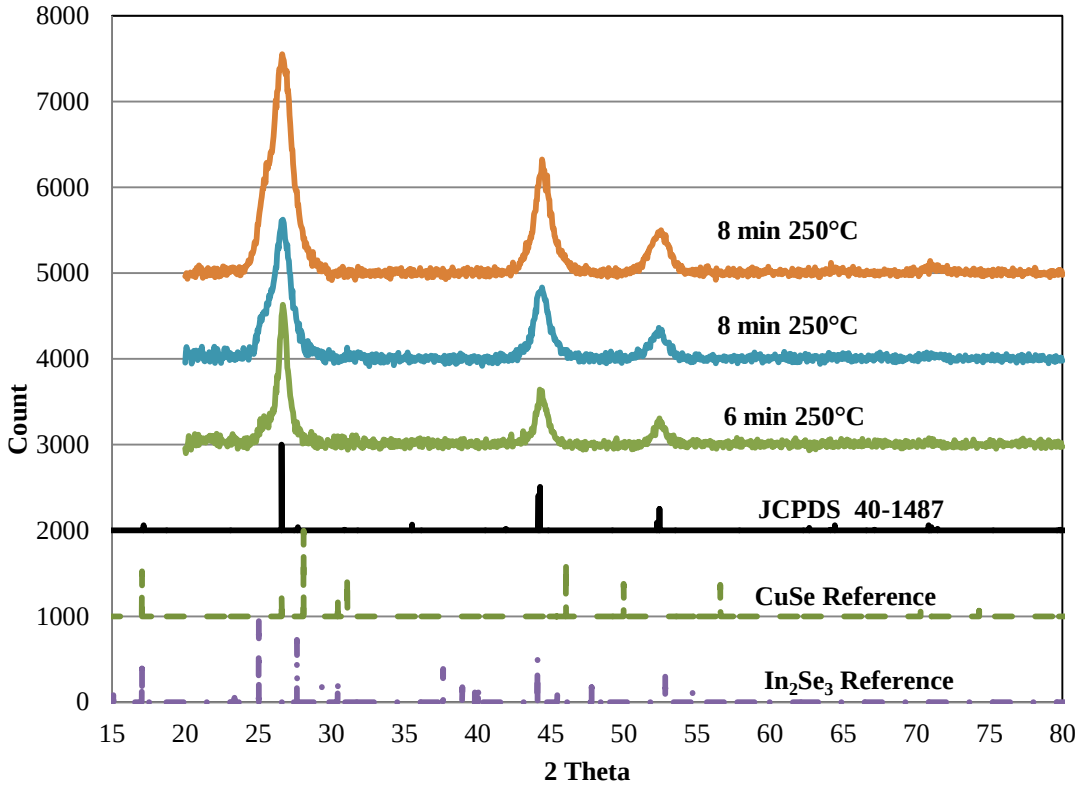

Figure 4.12 XRD of run 6 with increasing intensity of characteristic $CuInSe_2$ peaks.

In order to provide further confirmation of $CuInSe_2$ synthesis, Raman spectroscopy was completed for run 6. The Raman spectral response, Figure 4.13, provided an A_1 mode at approximately 175 cm^{-1} and 177 cm^{-1} for the two synthesis samples from run 6. The values obtained for the A_1 mode fit well with literature value for chalcopyrite $CuInSe_2$ nanocrystals[40, 41]. Although previous characterizations using XRD and EDX did provide responses that alluded to the

synthesis product being $CuInSe_2$, the results obtained for run 6 and shown in Figure 4.13, were the needed results to determine if the crystal structure of the $CuInSe_2$ was sphalerite or chalcopyrite. The XRD in Figure 4.12 lack the minor peaks at 17° and 35.6° that are representative of chalcopyrite and the EDX analysis provides elemental data which cannot be used to identify if the crystal phase was sphalerite or chalcopyrite. The blueshift in Figure 4.13 at 174 cm^{-1} was due to the size of the particles being around 9 nm in diameter[40, 41]. The weak response at 213 cm^{-1} was in good agreement with values that were predicted for $CuInSe_2$ modes[30, 40-42]. The weak response at 258 cm^{-1} can be due to CuSe intermediates, but the intensity of the peak was found to be relatively minor in comparison to the 174/177 cm^{-1} and 213 cm^{-1} modes that are characteristic of $CuInSe_2$. The peak at 110 cm^{-1} was unidentifiable through literature or selection of possible experimental components to $CuInSe_2$ or possible intermediates

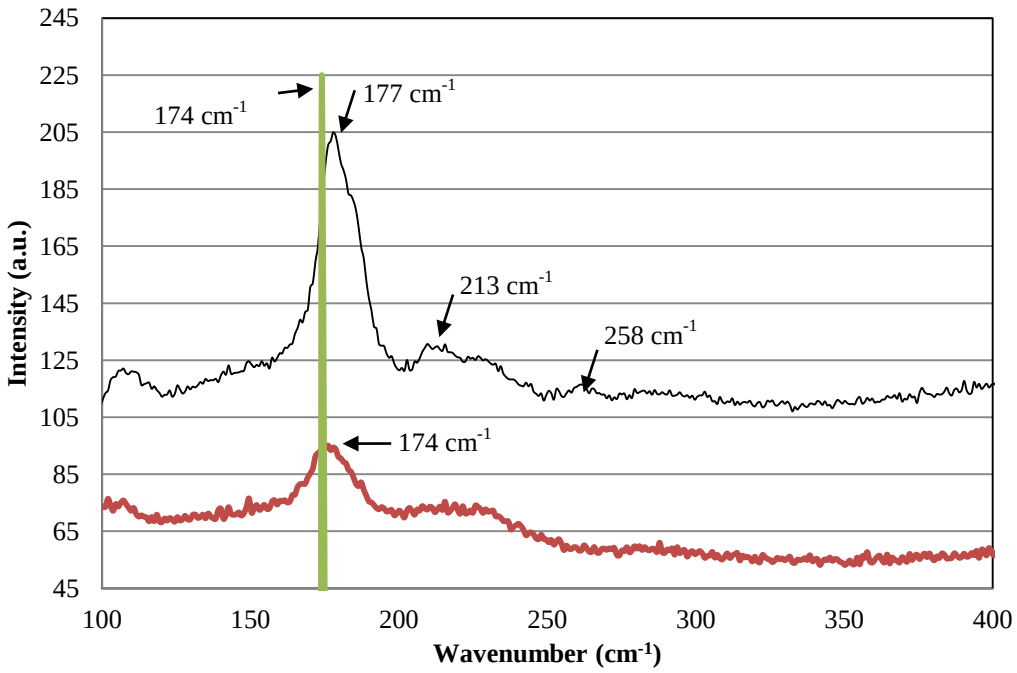

Figure 4.13 Raman results for injection temperature at 250°C and 8 minute residence time from run 6.

TEM imaging of run 6 samples resulted in the images of dispersed particles shown in Figure 4.14 at an 8 minute residence time. Several images were collected similar to that of the Figure 4.14 image, but agglomerates are still visible in Figure 4.17. Using Image J to measure the particles in Figure 4.14 (a) and (b), the average diameter was 6 nm as seen in Figure 4.16. The same triple wash and sonication method used previously for run 5 was also used for the run 6. Although agglomeration was a problem once again, the fact that dispersed particles were obtained showed that the agglomerates are composed of small particles as seen in Figure 4.14. Additionally, the results shown in Figure 4.14 help support the findings shown for run 5 in Figures 4.7 and 4.8, where small particles of about 5 nm were seen within the agglomerate.

The HRTEM result in Figure 4.16 for particle size agrees with Scherrer Equation results from Figure 4.12 as well. The size of the particles found from the Scherrer Equation was about 8 nm, whereas the size of the particles from Figure 4.14 was about 6 nm in diameter with a 1.2 nm standard deviation for a 20% coefficient of variation (COV) in Figure 4.16. An additional result for run 6 was a FFT of the HRTEM image from Figure 4.15. The spacing of the two diffraction spots (connected by the dotted line) in the FFT was found to be 0.19 nm, which fits well with the literature value of the d-spacing for the corresponding 44° (204/22) peaks (planes) found in XRD patterns such as Figure 4.12. SAED was completed to determine if the agglomerates were comprised of chalcopyrite $CuInSe_2$ as well for run 6. The result of doing SAED on run 6 can be seen with Figure 4.18. Similar to the results from the FFT diffraction pattern in Figure 4.15, the SAED results of Figure 4.18 provided d-spacings that fit well with the literature values for the first ring 26.6° (112), second ring 44.2° (204/220) and third ring 55.4° (116/312)[5, 13, 18].

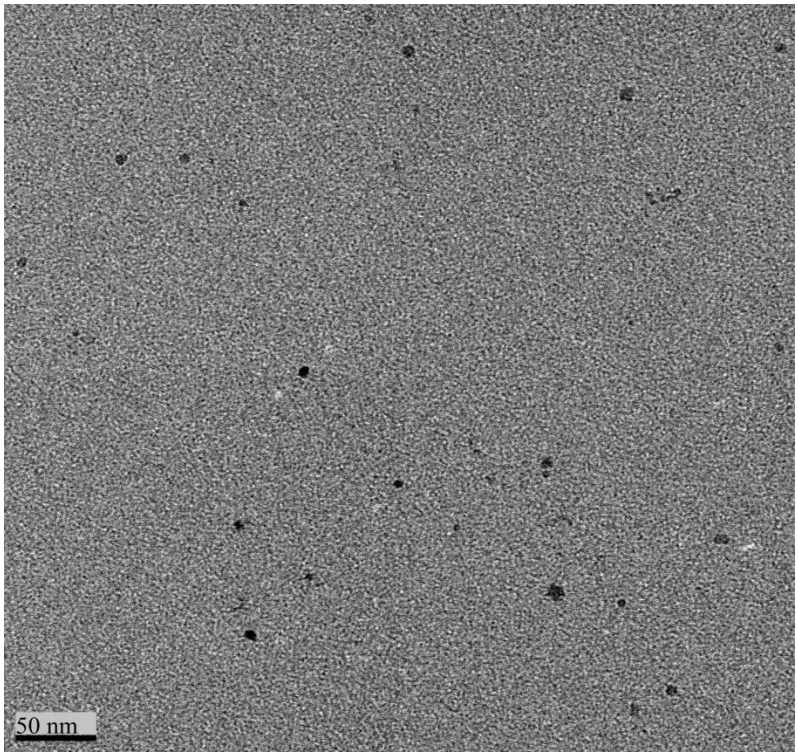

Figure 4.14 TEM image of dispersed particles for run 6.

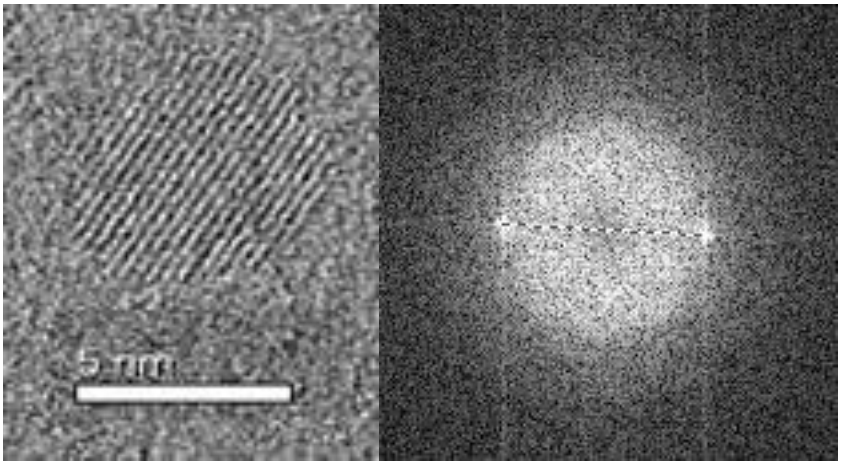

Figure 4.15 HRTEM and FFT of dispersed particle from run 6.

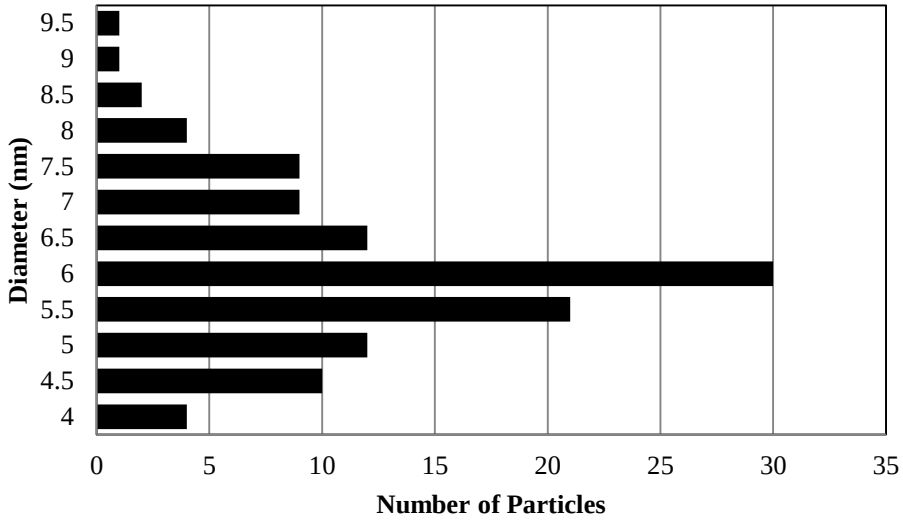

Figure 4.16 Size distribution histogram for particles from run 6.

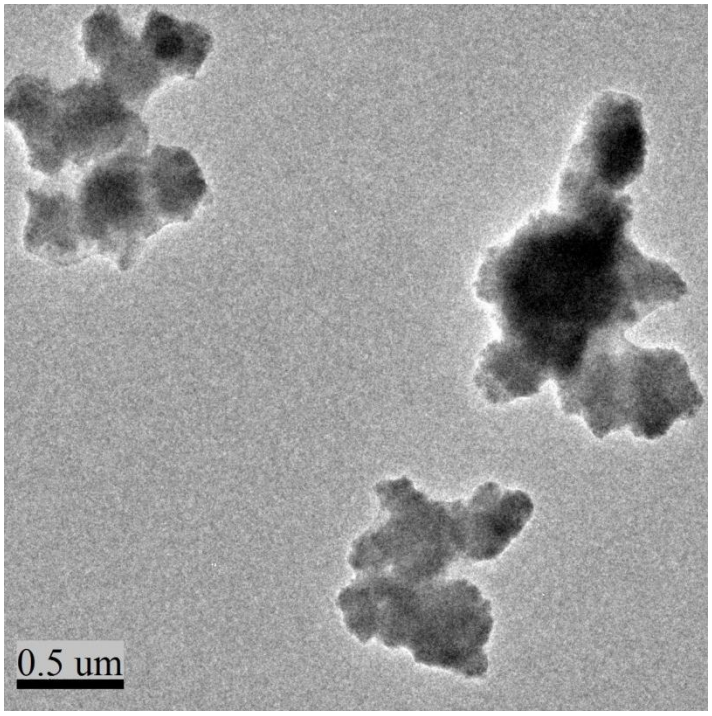

Figure 4.17 TEM image of agglomerated particles for run 6.

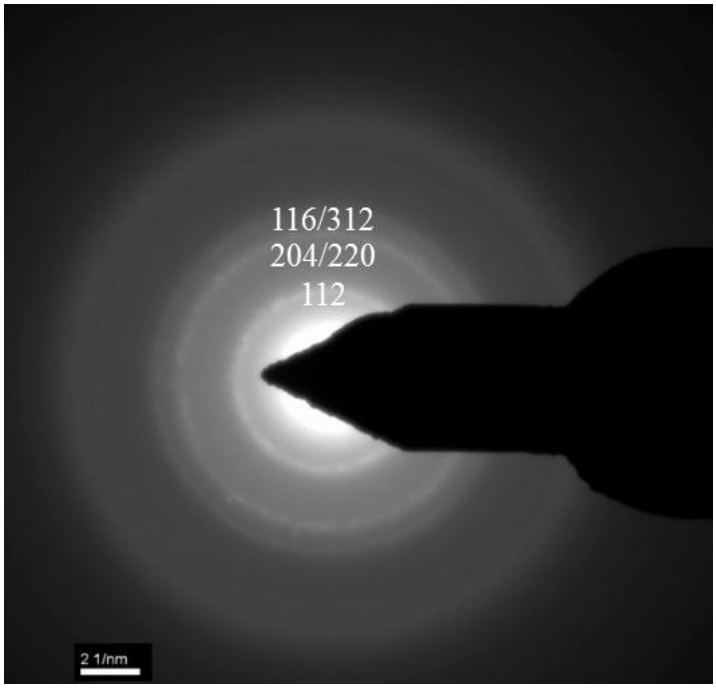

Figure 4.18 SAED of agglomerated particles from run 6

From the results presented up to this point, agglomeration was found to be the largest problem for all synthesized materials. As the injection temperature was increased to the nucleation temperature of $CuInSe_2$ and the growth temperature was increased to 250°C, the results of the crystal composition (and to a lesser extent particle dispersion) improved. Monodispersed particles, though, were not achieved at a desirable concentration. New recipes were employed in run 7 by reducing the OA:TOP ratio from 4:1 to 1:4 or zero OA concentration. The results of the zero concentration OA synthesis did not provide crystal synthesis. The effluent from the reaction system was of an orange-cream color that included a white precipitate. After two days the white precipitate dissolved into the solution, and thus the solution color changed to a clear orange. The lack of synthesis by only using the non-coordinating solvent TOP was found to support[5] and contradict[11] findings in literature. The OA:TOP synthesis for run 7 was conducted with a 1:4 by volume ratio did result in crystalline synthesis, as can be seen in Figures 4.19 and 4.20. The morphologies included spheres, rods, pyramids and irregular shapes, and size

distribution was wide. These results, by using TOP as the non-coordinating solvent, also fit synthesis runs that have been completed using 1-octadecene and octadecene[11]. Although the particles imaged below, Figure 4.19, were found to be a stable suspension in toluene, when they were placed onto a glass substrate for XRD characterization the particles' color turned from a black appearance to a white ash color in less than a half hour and without exposure to the XRD beam. Oxidation was assumed to be a problem with this sample and, for reference, this problem did not happen with any previous synthesis runs.

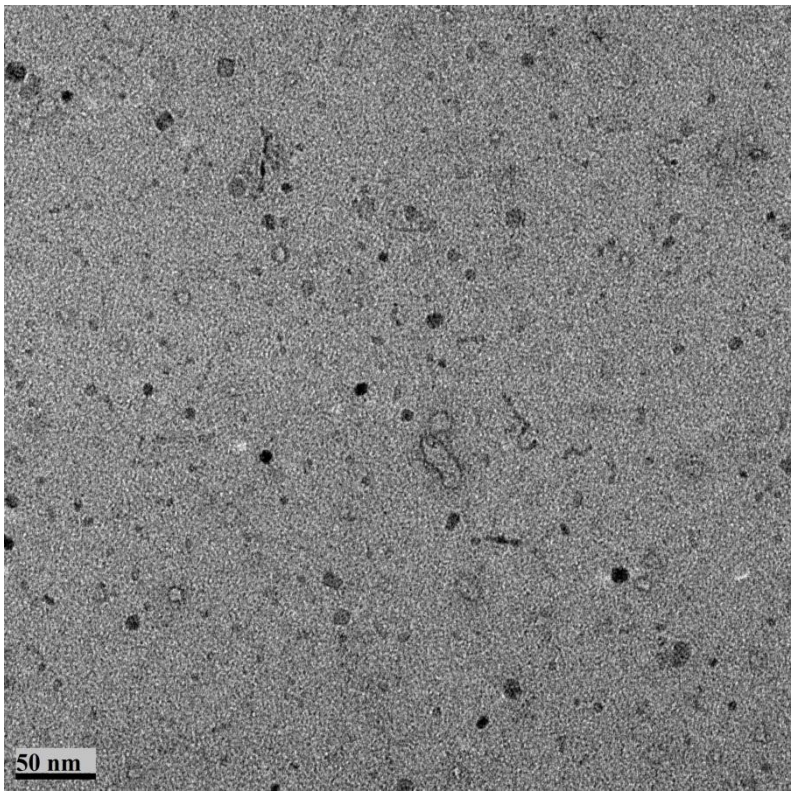

Figure 4.19 TEM of polymorph dispersed particles for run 7.

The results shown in Figure 4.19 and the lack of crystalline synthesis without including OA in the recipe provides insight into the role of OA as a ligand for $CuInSe_2$ synthesis. Synthesis for $CuInSe_2$ chalcopyrite phase was completed but the findings showed that the resulting nanocrystals had a wide size distribution, irregular shape and could not be dispersed in an organic solvent. Previous investigators,

however, were able to get monodispersed particles with excellent shape and size control[9, 22, 23], as well as other workers that reported problems with agglomeration[17, 20, 28, 43]. Not being able to produce monodispersed particles with size and shape control is a result of several potential factors. One potential factor can come from the precursor thermal decomposition not providing the necessary reaction to create a high concentration of active atomic species that is required for a sudden nucleation event. As was mentioned previously, in Chapter 2, if the nucleation event does not quickly build nuclei then a wide distribution of particle sizes will be produced. From this, large particles would continue to grow and small particles would reduce in size. A more probable scenario for a lack of monodispersed particles is that OA does not properly cover the surface and/or does not have sufficient binding energy to remain on the surface of the $CuInSe_2$, which means during the washing process the OA is removed from the surface and the nanocrystals aggregate to one another via Van der Waals forces causing the persistent agglomeration results.

Although monodispersed particles were not obtained at desired concentrations, the utilized continuous precursor thermal decomposition method did provide proof of concept that chalcopyrite nanocrystals can obtained and as seen within Figures 4.7 and 4.14 small crystals can be obtained. The most probable cause for agglomeration was hypothesized to be OA not being a sufficiently effective capping surfactant for $CuInSe_2$ synthesis.

4.2 PbS Synthesis

The current work on PbS is an extension of the work discussed previously by Hines and Scholes[14]. Synthesizing PbS was chosen due to a bulk band gap of 0.41 eV and an exciton Bohr radius of 18 nm[4, 14]. Additionally, lead chalcogenides have an inherently large Bohr radius that makes PbS quantum dots desirable for use in optical devices such as light emitting diodes (LEDs) due to enhanced quantum confinement energies[14, 44]. Synthesis of binary PbS nanocrystals was chosen in order

to show an extended proof of concept using a continuous flow system. As was mentioned in the background section for PbS synthesis, the synthesis technique used for these experiments follows that of the previous work completed in the research group[15] with the recipe adopted from Hines and Scholes[14]. The parameters investigated for the PbS nanocrystal synthesis was injection and growth temperature, residence time and concentration of the coordinating solvent, OA. Synthesis runs were completed as seen in Table 4.3. Run 1 and run 2 were done with an OA volume of 20 mL, whereas runs 3 and 4 were completed with 1.5 mL of OA and 18.5 mL 1-ODE in the lead oleate precursor.

The XRD results for run 1, Figure 4.20, show a general trend that the intermediate (PbO) at the 64° peak increases as residence time increased. An impurity that could not be identified at 37° became less pronounced as residence time increased. The major characteristic peaks for PbS at 25.9° (111), 30.1° (200), 43.1° (220), 50.9° (311) and 53.4° (222) were present along with secondary peaks of 62.5° (400), 68.8° (331) and 70.9° (420). The crystal structure of PbS matches closely with that of the face-centered cubic (fcc). The peak at 64° closely resembles PbO but without the other characteristic PbO peaks present, the 64° peaks is most likely an impurity like that at 37°.

Table 4.3 PbS synthesis runs

Run #	Injection Temperature (°C)	Growth Temperature (°C)	Residence Time (min)	Other	Figure (F) or Table (T) #'s
Run 1	20	130	2.5, 5, 10	Lab Alliance pumps, Stainless steel tubing for Lead Oleate precursor	F 4.21-4.23
Run 2	20	90, 100, 130	2.5	KD Scientific Pump Viton/Tygon tubing	F 4.24-4.29
Run 3	~90	90, 100, 120	2.5	KD Scientific Syring pump, Viton/Tygon tubing, reduction of OA volume from 20 mL to 1.5 mL. Inclusion of 18.5 mL 1-ODE in lead oleate precursor	F 4.30-4.37
Run 4	~90	90, 100, 120	2.5	Peristaltic pumps, Viton/Tygon tubing, reduction of OA concentration from 20 mL to 1.5 mL. Inclusion of 18.5 mL 1-ODE in lead oleate precursor	F 4.38-4.43

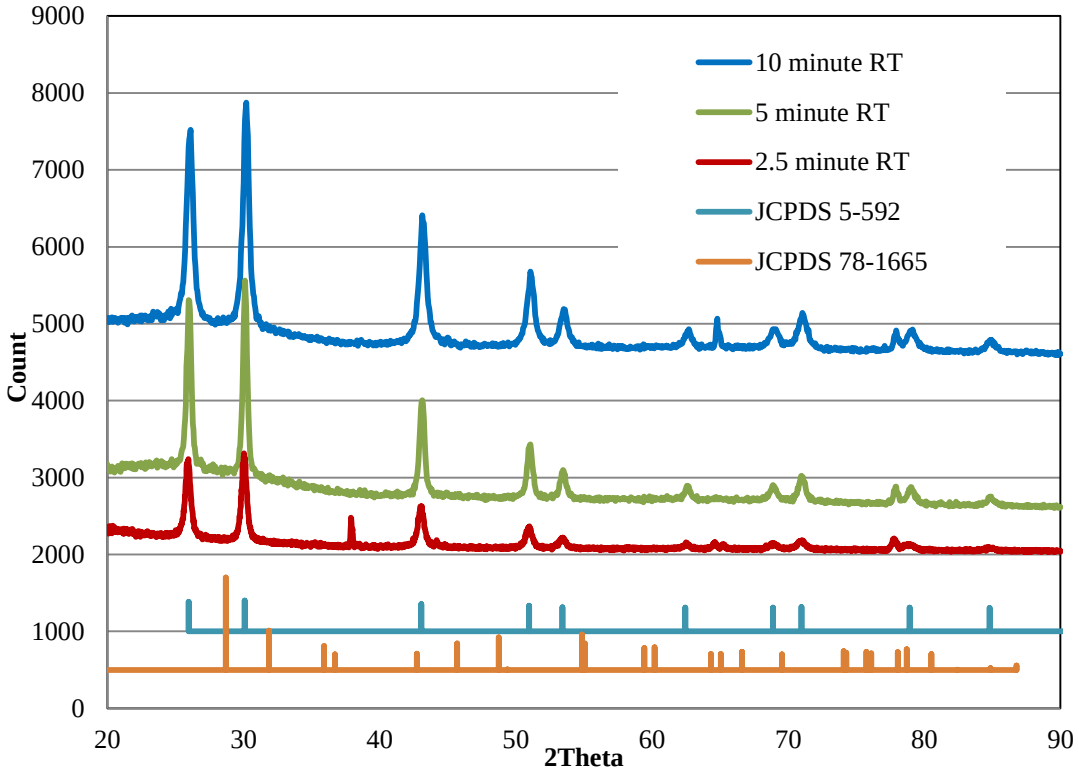

Figure 4.20 XRD run 1 with characteristic PbS peaks.

The Philips CM-12 TEM imaging of run 1, Figure 4.21, shows the particles produced from a 5 minute residence time. The crystals appear to be cubic in shape and were measured to be approximately 15 nm to 22 nm in size. The cubic structure of the nanocrystals fits well with reported synthesis results[45-47]. Additional imaging of run 1, shown in Figure 4.22, for a 2.5 minute residence time produced nanocrystals that are not aggregated but also appear to be more spherical than those of the nanocrystals synthesized for Figure 4.21, although this observation comes with a cautious assumption due to the lack of resolution apparent in the image. The change from spherical to cubic nanocrystals has been researched and discussed within literature[48, 49]. Crystal transformation from spherical to cubic within the reaction system and recipe used can be due to preferred growth of the PbS active atomic species into a crystal structure, from initially spherical, into the more thermodynamically favorable cubic shape[14, 49].

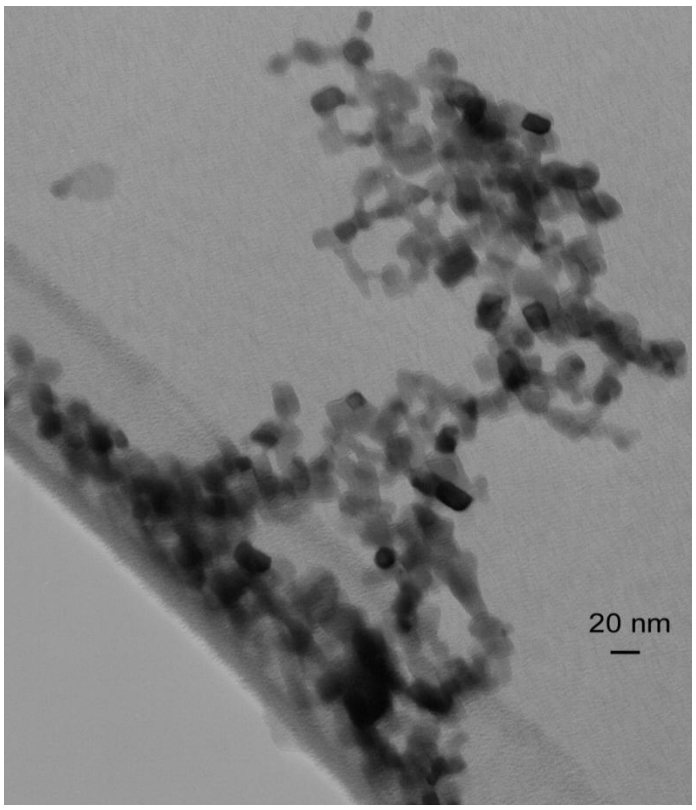

Figure 4.21 TEM image of PbS nanocrystals for run 1 at a 5 minute residence time.

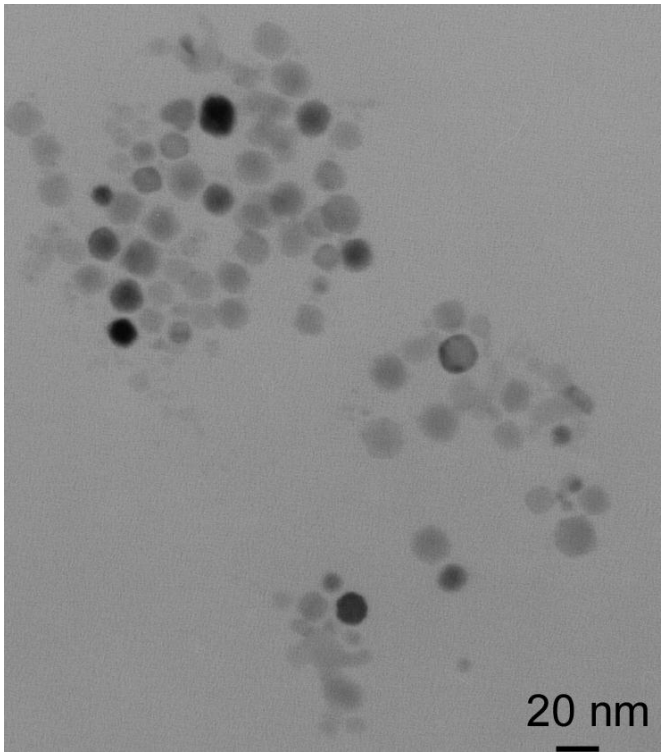

Figure 4.22 TEM image of PbS nanocrystals for run 1 at a 2.5 minute residence time.

The next synthesis parameter that was investigated was the effect of growth temperature in run 2. The motivation for examining growth temperature was to investigate if particles approximating a spherical shape could be more easily obtained while also decreasing the size of the nanoparticles to less than the 20 nm size found in run 1.

The XRD of run 2 in Figure 4.23 indicates that as the growth temperature increased the XRD peak intensity increased and the width narrowed. This indicates that the bulk crystal size was increasing, which was also noted with the synthesis of $CuInSe_2$ nanocrystals discussed previously. Additional analysis of Figure 4.24 indicates that the PbO intermediates that are seen at 48°, 65° and 69° are no longer present when a the final growth temperature of 130°C is used. These results indicate that the nanocrystals synthesized were PbS. The peaks at 37° and 64° from run 1 in Figure 4.20 were not present with run 2 in Figure 4.23. As was found with $CuInSe_2$

synthesis the precursors used in synthesizing PbS have a leeching effect on stainless steel tubing and in run 2, the stainless steel pump head and tubing was removed. The end result was that no impurity peaks are seen in run 2, unlike in run 1.

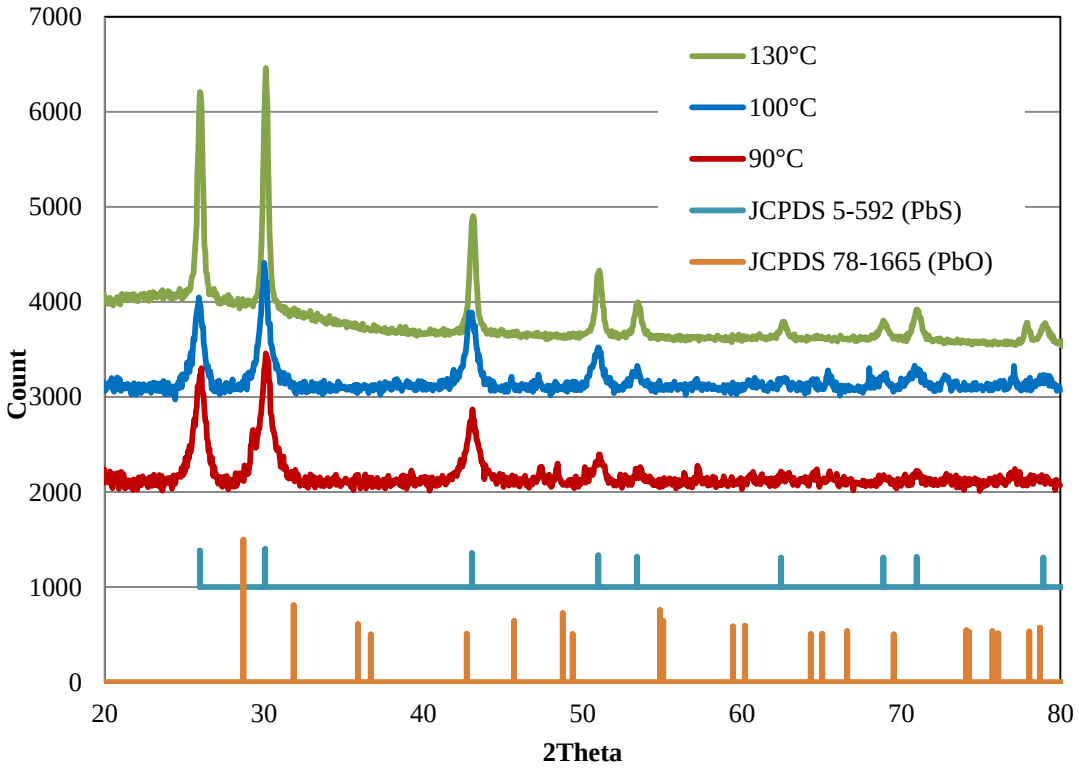

Figure 4.23 XRD of run 2 with characteristic PbS peaks.

Images up to this point were limited to the TEM images of Figures 4.21 and 4.22 from a Phillips CM-12 low-resolution TEM, however Figures 4.24, 4.26 and 4.27 show the results of HRTEM and FFT. Size distribution analysis of the particles in Figure 4.24 was completed by measuring particles using Image J with the results found in Figure 4.25. Run 2 provided a normalized and narrow size distribution with approximate shape uniformity using a continuous process with OA as the surfactant for coordination.

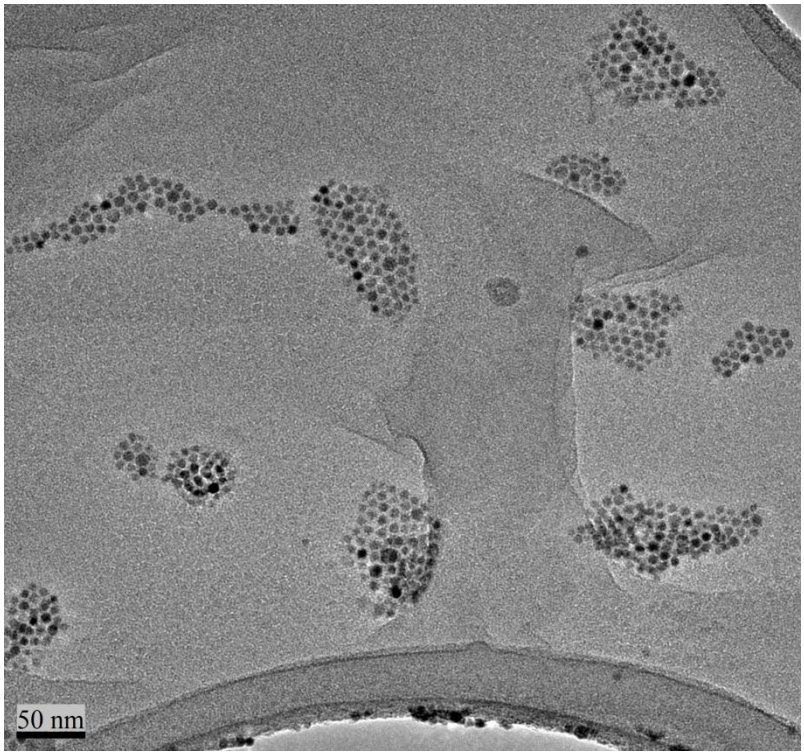

Figure 4.24 TEM images of PbS nanocrystals grown at 100°C.

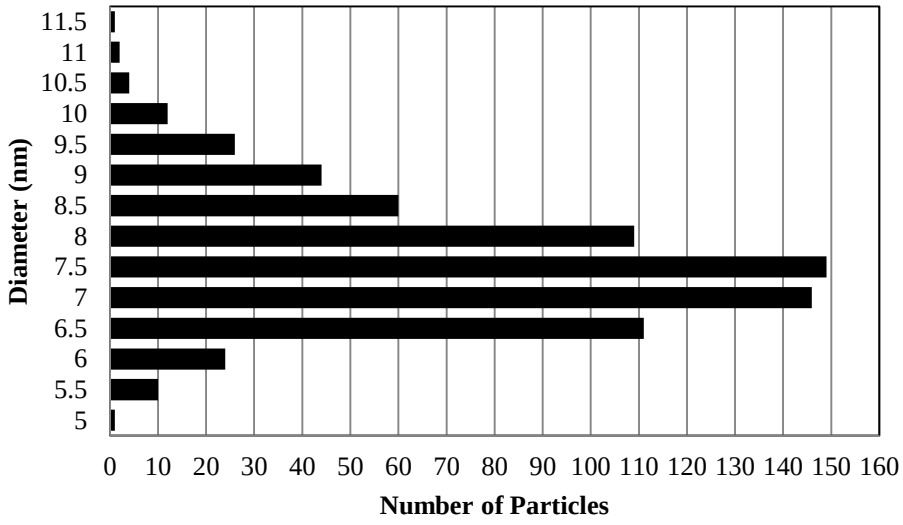

Figure 4.25 Run 2 size distribution of PbS particles grown at 100°C.

The results of low magnification TEM imaging, as shown in Figure 4.24, indicate that particle shapes approximates those of sand grains. For the 100°C growth temperature 700 particles were measured using Image J. The distribution of the particles ranges from 5 nm to 11.5 nm with an average of 7 nm and a standard deviation of 1 nm for a COV of 14%. Only one significant figure is reported due to the inherent error of measuring the nanoparticles. The size of particles from the Scherrer Equation was found to be approximately 10 nm in Figure 4.24. The XRD sample was taken from the dry centrifuge sediment, whereas the TEM sample was drop-cast from suspended particles in a dilute toluene solution. Bulk particle size may be closer to 10 nm rather than the 7 nm value found with the TEM images.

In addition to the low-magnification images, HRTEM was completed as seen in Figures 4.26 and 4.27 for run 2. The particle circled in black within Figure 4.26 was used for the FFT function with Image J to determine the lattice spacings of the particle. The measured lattice spacing of the particle was found to be 0.3 nm which correlates well with the 200 diffraction plane for the PbS fcc crystal structure and agrees well with reported findings[14, 45, 48]. Additionally, the particle in Figure 4.27 appears to be well aligned with the 100 plane of the PbS unit cell due to the alignment of the PbS atoms[50]. The clarity of the lattice spacings indicate a lack of stacking defects or dislocations providing for a pure crystalline PbS particle. The FFT indicates that the diffraction pattern fits closely with the 200 (30°) and 220 (43.1°) planes[48, 51, 52]. As can be seen in Figure 4.26, there was a size distribution of particles, but the sizes still remain within the values found for the size distribution in Figure 4.25. Close observation of the particles in Figure 4.26 shows that the edges of the particles appear to be more polycrystalline rather than monocrystalline. Looking at the results of run 1 and 2, as the crystals grow the shape of the crystals becomes defined, from spherical/grain-like (polycrystalline) to cubic with distinct crystal edges (monocrystalline).

Compositional analysis, EDS, completed on material synthesized in run 2 showed that the results indicated that material synthesized was approximately

$Pb_{1.25}S_{1.00}$ over three different selected areas. A possible factor for a lack of 1:1 molar ratio of Pb:S can be seen in Figure 4.28, where the major response for sulfur is also a peak indicative of lead. How much that peak should be attributed to sulfur or lead was not able to be determined. On the surface of the sample prepared for EDS in Figure 4.28, there is most likely some synthesized PbO as well due to the minor oxygen response. Regardless, HRTEM/SAED and XRD results do show that the synthesized particles represent the PbS fcc crystal structure and the EDS results can be more closely associated to the desired 1:1 ratio. The next parameter investigated was the effect of changing from a lead oleate precursor with 20 mL of OA to a precursor with 1.5 mL OA and 18.5 mL ODE (non-coordinating solvent).

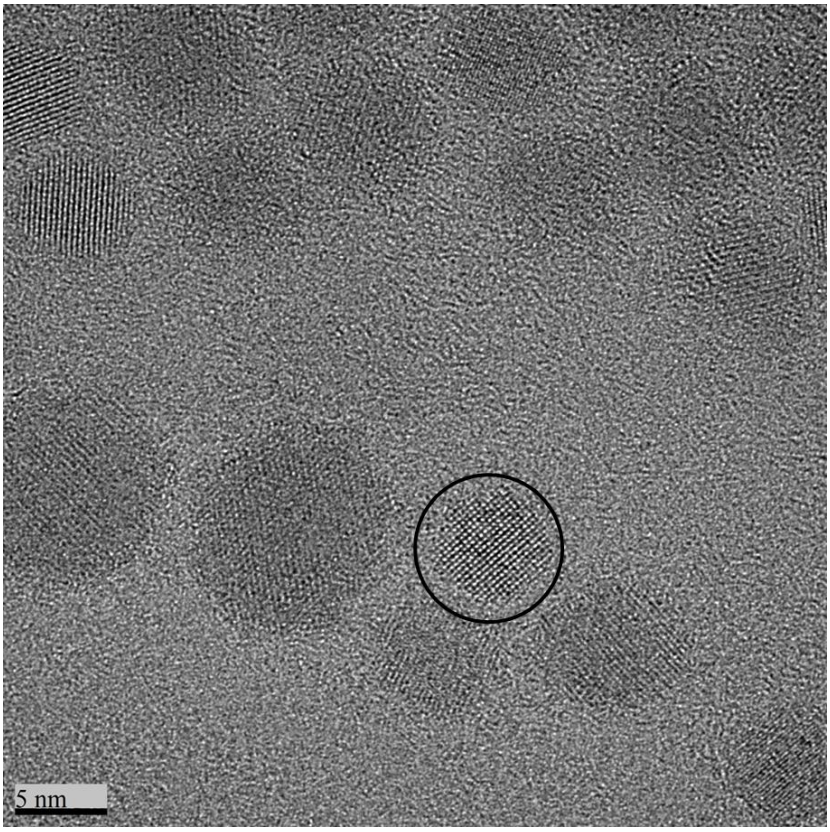

Figure 4.26 HRTEM of PbS nanocrystals synthesized at 100°C from run 2.

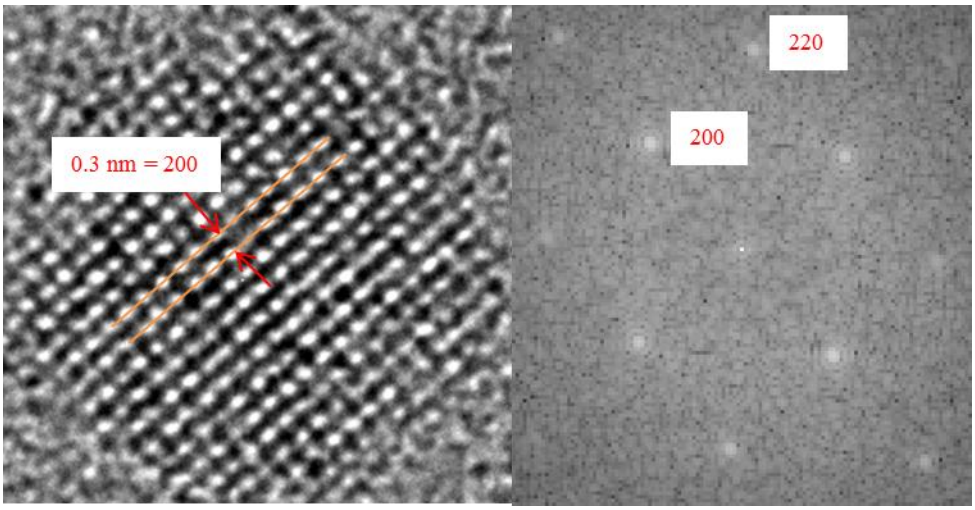

Figure 4.27 HRTEM and FFT image of PbS nanocrystal grown at 100°C from run 2.

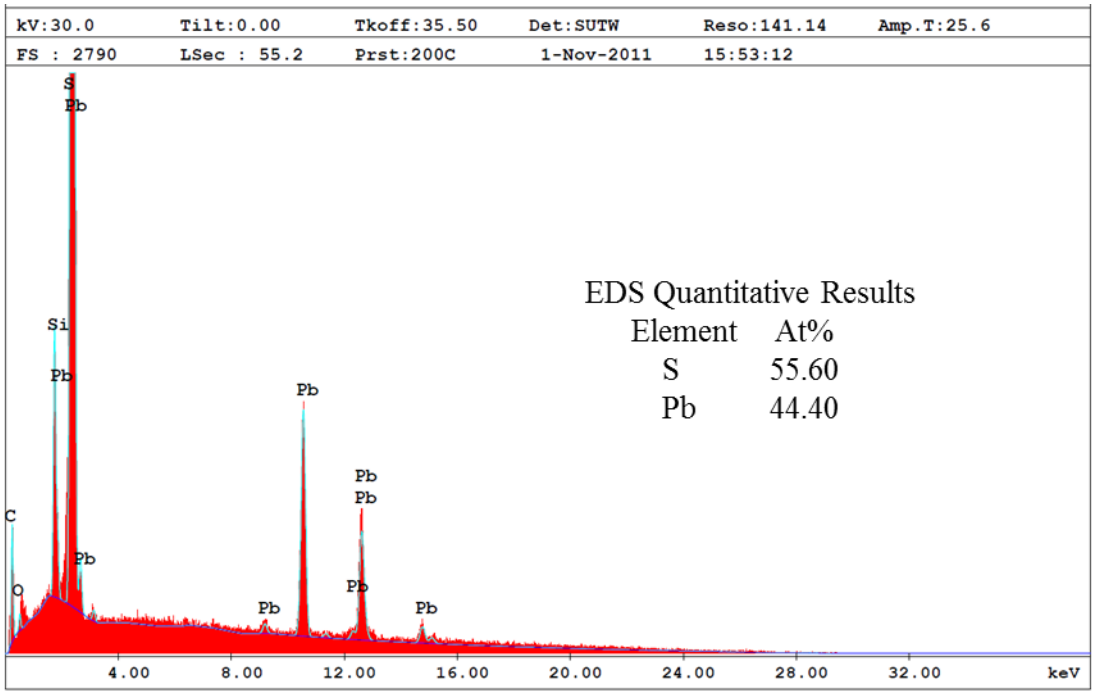

Figure 4.28 EDS of PbS material from run 2

The results from run 3 can be seen in Figures 4.29 through 4.37. Before discussing the results further, the analysis must be prefaced with the fact that the particles produced were made in a different manner. The lead oleate precursor vial was at an elevated temperature, the exact temperature was not recorded but the vial

was uncomfortably hot to the touch. The $(tms)_2S$ precursor was then injected directly into the hot lead oleate precursor. Immediately after injecting the $(tms)_2S$, the solution turned from a clear yellow color to a dark brown[7, 14]. Pumping from the lead oleate $(tms)_2S$ vial was then started, and the growth temperature was adjusted to 90°C, 100°C or 120°C for the growth zone. Prior synthesis runs mentioned earlier resulted in black precipitates and black solution, but changing the concentration of OA resulted in a dark brown solution in which precipitation was found to be minimal[7, 53].

As can be seen from Figure 4.29 and 4.30 the particles are well below 20 nm, which can also be seen in the size distribution Figures 4.31 (100°C growth) and Figure 4.32 (120°C growth). A difference of 20°C in growth temperature provided roughly 1 nm in diameter increase in particles size as can be seen from Figures 4.31 and 4.32 where the average particle size was found to be 3 nm and 4 nm, respectively. This helps to demonstrate the necessity of considering growth temperature as an important parameter for synthesizing monocrystalline PbS particles on a larger scale. One problem with the particles synthesized in Figures 4.29 and 4.30 would be the lack of uniform shape. The particles are clearly asymmetric and further demonstrate that as the crystals grow the polycrystalline behavior tends to rearrange to form monocrystalline particles. Despite a lack of significant difference visually with the particles from Figures 4.24, 4.26, 4.29, and 4.30, measuring the particles with Image J was not as clear-cut as measuring from Figures 4.24 and 4.26. With Figures 4.24 and 4.26 the particles shape was more clearly defined, whereas for Figures 4.29 and 4.30 measuring the diameter required approximating the point along the perimeter that would result in the greatest value for diameter.

With the sudden color change seen upon injecting $(tms)_2S$ into the hot lead oleate, the suggestion is that upon injection there was a sudden burst of active atomic species of PbS which led to active atomic species quickly forming small particles and consequently the active atomic species concentration approached minimal

concentrations. With a large concentration of well capped small particles and most likely a lack of concentration of active atomic species, the growth of particles as seen in Figures 4.29 and 4.30 was minimal[2, 3, 14].

Despite the lack of uniform shape, the resulting particles that were measured provided a narrow particle size distribution as seen in Figures 4.31 and 4.32. Additionally, the HRTEM images, Figures 4.33 and 4.34, provided results that matched the findings from Figures 4.26 and 4.27 for run 2 as the lattice spacing was found to be 0.3 nm which corresponds to the 200 diffraction plane for PbS fcc crystal structure for a 100°C growth temperature.

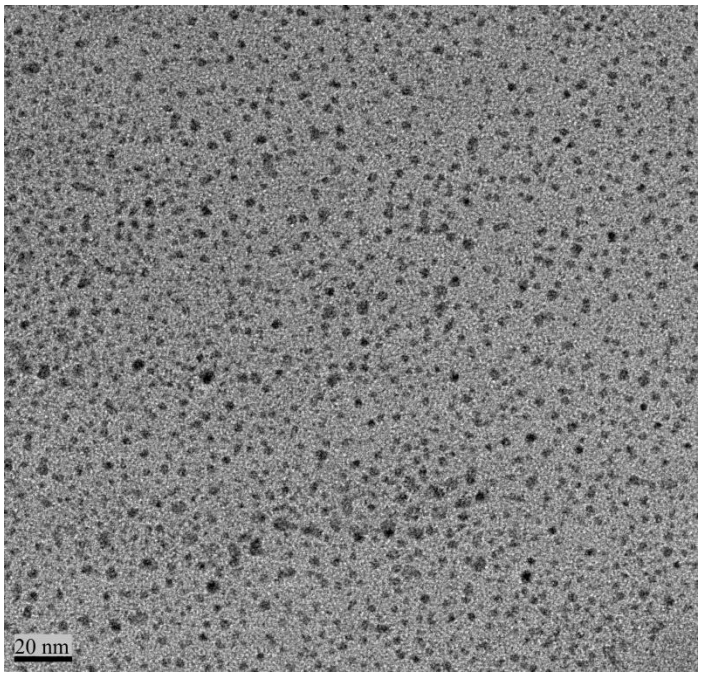

Figure 4.29 TEM image of PbS nanocrystals for run 3 at 100°C.

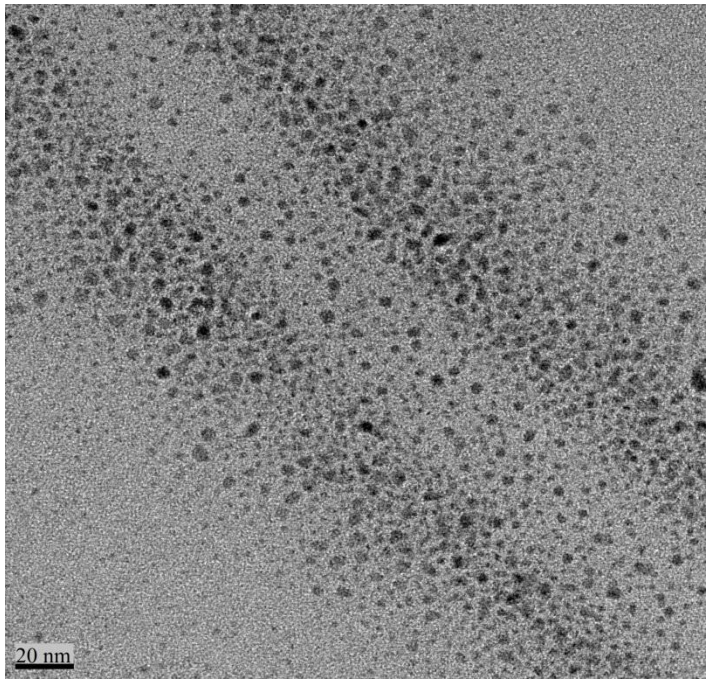

Figure 4.30 TEM images of PbS nanocrystals of run 3 at 120°C

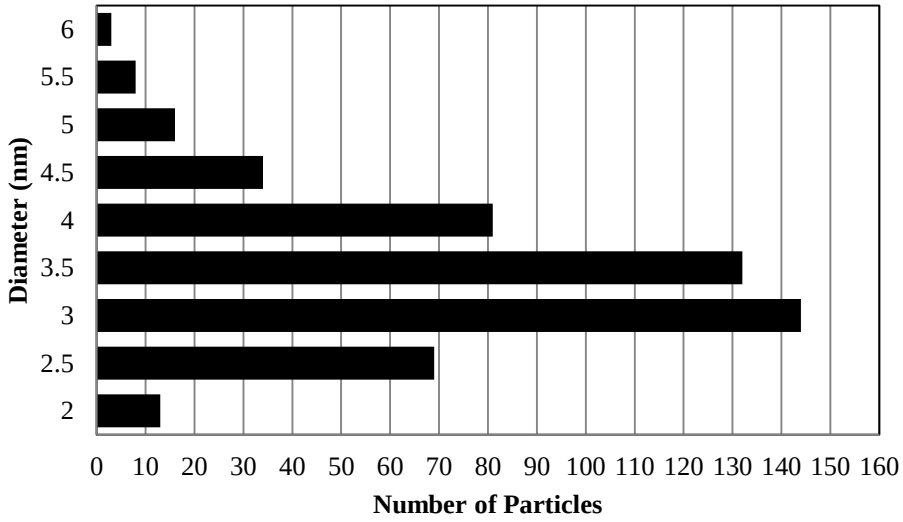

Figure 4.31 Run 3 size distribution of PbS particles grown at 100°C.

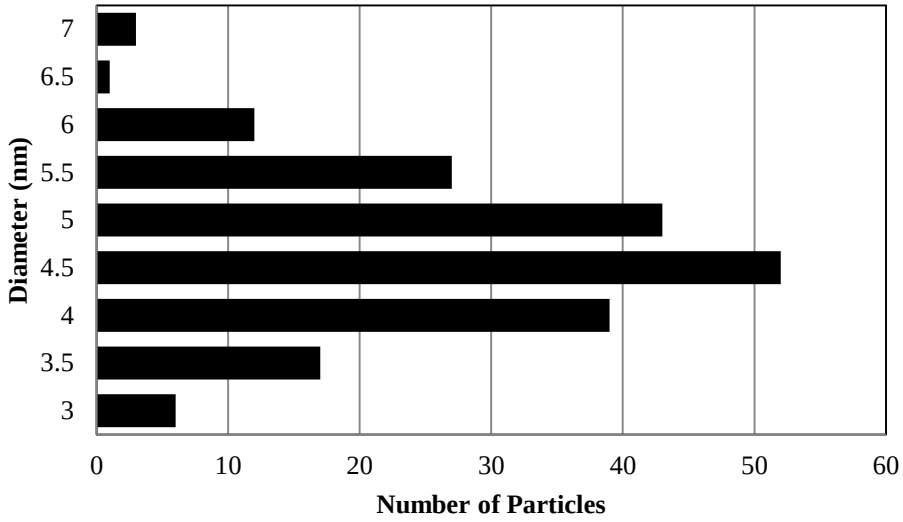

Figure 4.32 Run 3 size distribution of PbS particles grown at 120°C.

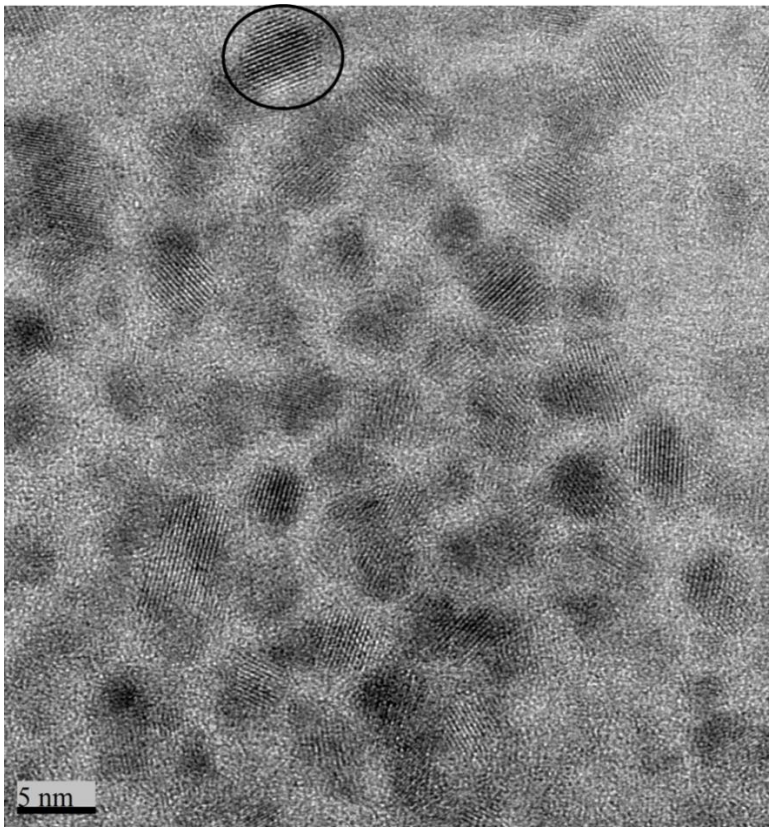

Figure 4.33 HRTEM of PbS nanocrystals synthesized in run 3 at 100C°.

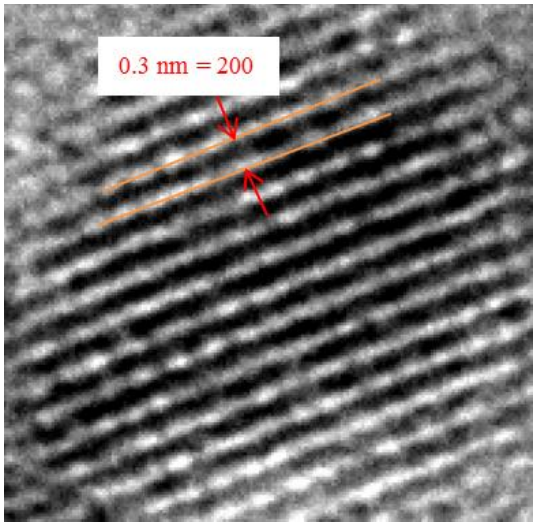

Figure 4.34 Close up of PbS nanocrystal circled in black in Figure 4.34.

In order to fully understand the results obtained with the change in concentration of OA, UV-VIS was used to investigate the optical properties of the PbS nanocrystals that were synthesized. The absorption spectra for the particles are show in in Figure 4.35. An absorption onset at approximately 700 nm can be seen, which was a large blueshift compared to the 3,020 nm (0.41 eV) for that of bulk PbS. The value for the absorption does agree with that obtained from previous works[7, 14, 54, 55]. Due to a lack of distinct growth of the particles from 100°C and 110°C growth temperature, the difference in the onset for the two temperatures investigated can be seen as minimal in Figure 4.35. The values for bandgap are all above 3.0 eV, which was about a 7 fold blueshift compared to the 0.41 eV value for bulk PbS. Other work has also shown blueshifts but the values never exceeded 2.0 eV[50, 54-56]. Theoretical modeling in literature also shows that for particles sizes of 3nm, the bandgap value is 2.0 eV[44, 57]. Although the large estimated bandgap values are not what was, or should be expected, the fact that the synthesized particles provided for an absorption onset peak around 700 nm did fit closely with the results obtained in other work, although the absorbance in Figure 4.36 is less pronounced than the work of Hines and Scholes[14]. The particles produced via a thermal decomposition batch

method resulted in similar dark brown/red precipitate that remained suspended in toluene[14].

Characterization by photoluminescence (PL) shows that the emission peak increases with increased growth temperature. Additionally, the full-width at half maximum (FWHM) shows that the shift from exciton to emission becomes greater in value with increased growth temperature. The FWHM from the absorbance was calculated to be 265 meV and 280 meV for 100°C and 110°C growth temperature respectively. The relatively broad peaks for PL indicate that there were possible trapped state emissions unlike that from reported literature for similar conditions[7, 14, 52]. The broadened emission peak seen in Figure 4.35, implicates that the size distribution of the particles in solution was not as narrow as that of published works. A broadened peak implies particles of different sizes causing emissions over a wider range of wavelengths.

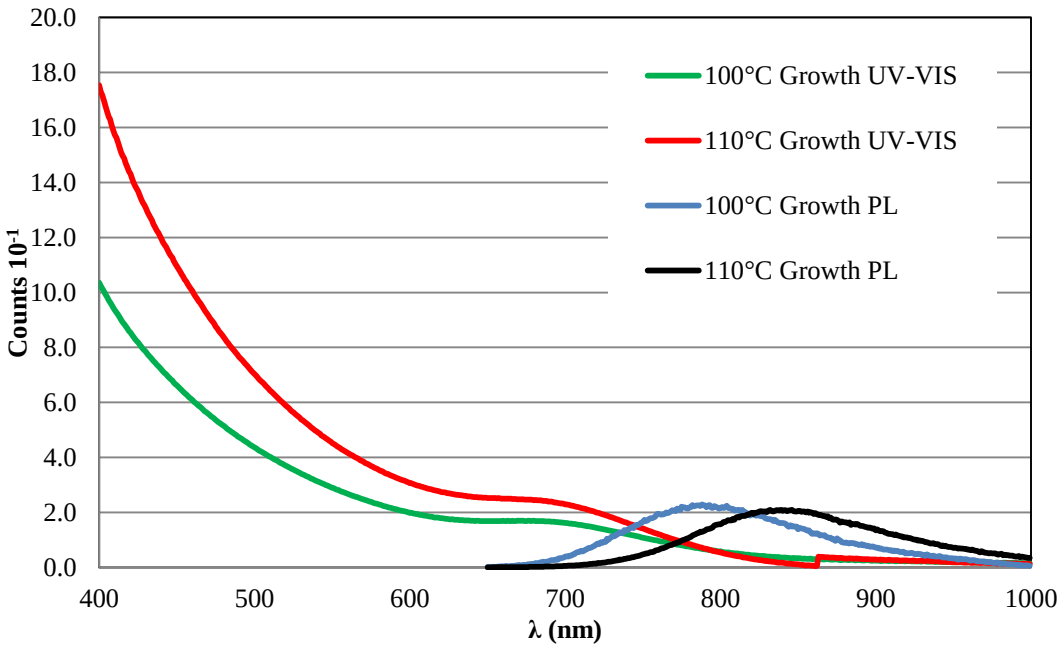

Figure 4.35 UV-Vis and PL results of PbS nanocrystals from run 3.

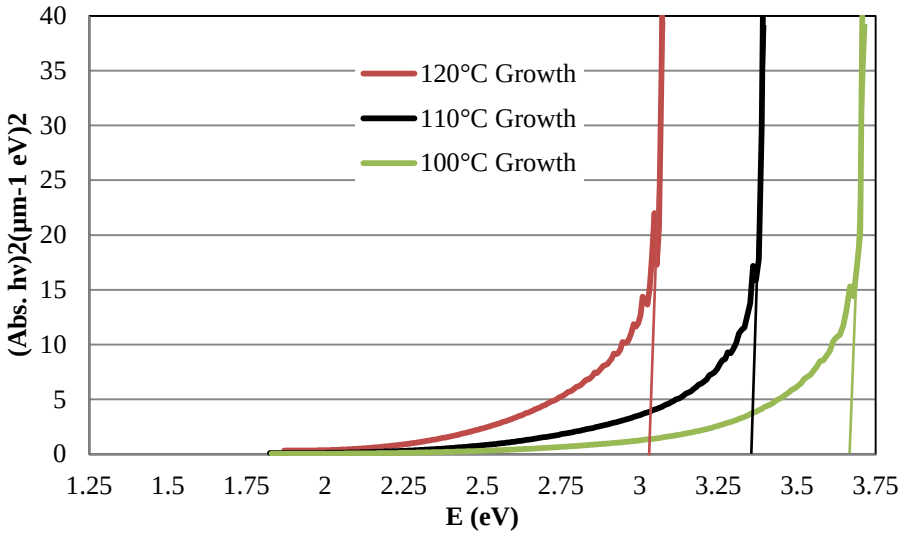

Figure 4.36 Fitted absorbance data for determining bandgap energy for run 3.

To conclude the PbS work run 4 experimental conditions were formulated, this time the $(tms)_2S$ was not injected into the lead oleate precursor prior to pumping. Rather the lead oleate was pumped through the pre-heating zone as described in Chapter 3, Figure 3.1. The injection temperature was 90°C with the growth temperature ranging from 90°C (Figure 4.37 and 4.39) to 120°C (Figure 4.38 and 4.40).

The resulting particles from run 4 can be seen in Figures 4.37 and 4.38. The size distribution from Image J measurement shows that the sizes of the particles are less than 10 nm, Figures 4.39 and 4.40. For the 90°C synthesis the average particle diameter was found to be 3 nm in Figure 4.39, whereas for 120°C condition the average was approximately 7 nm in Figure 4.40. The results were slightly different than those shown in Figures 4.31 and 4.32, where the average diameters were 3 nm and 4 nm, respectively. From Table 4.3, the difference using a syringe pump for run 3 and two peristaltic pumps in run 4 leads to a conclusion that injecting the $(tms)_2S$ precursor into the lead oleate prior to pumping in run 3, the particles are able to grow suddenly and prevented any growth from occurring due to a capping effect on the particles. By injecting the $(tms)_2S$ into the lead oleate within the flow cell in run 4,

there was still a large active atomic species concentration following the nucleation event which resulted in a subsequent growth event where residual active atomic species diffused to the surface of the PbS particles.

Once again the shapes of the particles are not uniform like those of the previous runs where the shape appeared to be roughly spherical or cubic. As has been reported in literature[14], the results of symmetric shapes was a result of longer residence times or higher growth temperatures (130°C versus 90°C) for run 1. Asymmetric particles were a result of lower growth temperatures or shorter residence times in runs 2, 3 and 4. One takeaway would be that the highly reactive $(tms)_2S$[14, 58] creates a sudden nucleation event and the high concentration of active atomic species appears to prefer growth on the 111 face of the PbS crystal structure due to OA being a weakly bound ligand. Since OA binds weakly to the PbS structure, the 111 face grows much faster and as a result of being at lower growth temperatures or shorter residence times the PbS particles are asymmetric[14]. As a result of elevated growth temperatures or longer residence times, the enhanced exposure to heating did smooth the shape of the particles and correlates well with literature[14, 46, 47, 59]. Residence time at growth temperatures is critical in order to produce quality PbS nanocrystals that have a narrow size distribution and also a uniform shape. The residence time in a continuous flow microreactor needs to be relatively long and/or the thermal input needs to ensure sufficient heating for sudden nucleation and desired particle growth. Another possible parameter for changing the growth characteristics would be changing the ligand from OA. Changing to a strong ligand could limit growth to the point of where the particles would be uniform in shape. This recommendation is based on the results obtained here for PbS and also the highly agglomerated particles obtained for $CuInSe_2$ synthesis.

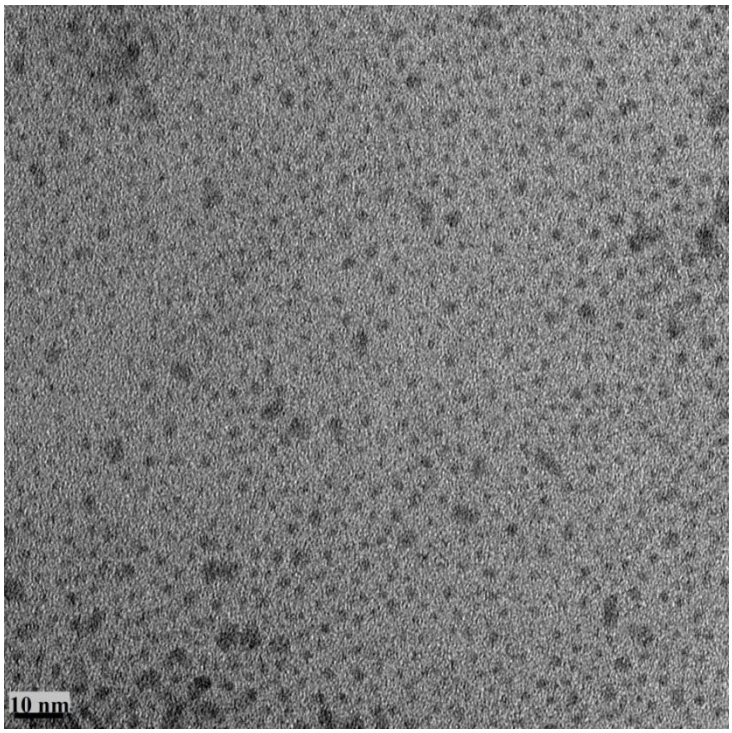

Figure 4.37 TEM image of PbS nanocrystals grown at 90°C from run 4.

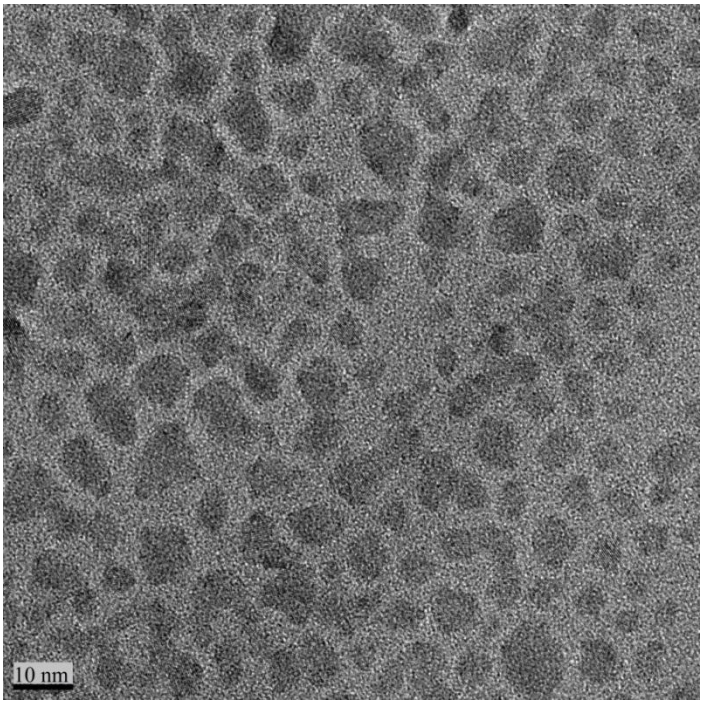

Figure 4.38 TEM image of PbS nanocrystals grown 120°C from run 4.

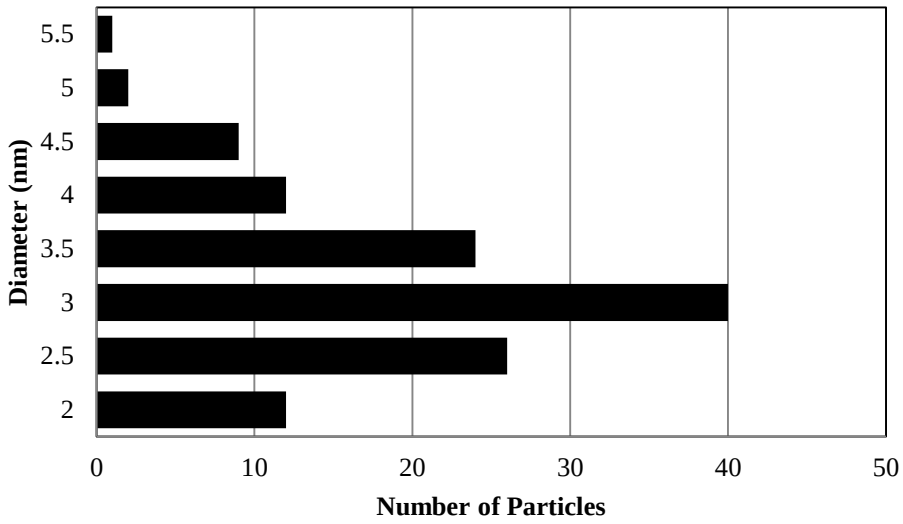

Figure 4.39 Run 4 size distribution of PbS particles grown at 90°C.

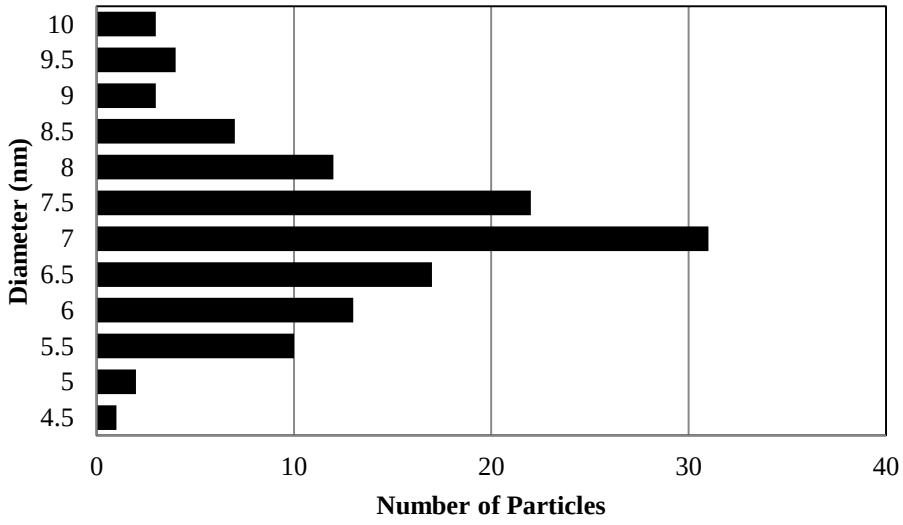

Figure 4.40 Run 4 size distribution of PbS particles grown at 120°C.

UV-VIS was used once again in order to investigate the optical properties of the synthesized PbS nanocrystals. From Figure 4.41 the absorption spectra for the particles demonstrated an absorption onset at approximately 600 nm, which was once again a large blueshift compared to the 3,020 nm (0.41 eV) for that of bulk PbS. Despite the apparent change in the growth of the particles shown in Figures 4.38 and

4.39, the absorption onset was not as pronounced as the theory for quantum confinement would assume. The difference in the absorption onset for the temperatures investigated was found to be minimal, as was found in run 3. The particles that were synthesized provided for an absorption onset around 600 nm that did fit closely with the results obtained from other published work[14]. The plotted absorbance spectrum shown in Figure 4.42 shows the effect of the blueshift on the value for bandgap when extrapolating from the steepest point to zero absorbance in order to find bandgap. The bandgap values are approximately 2.4 eV, 2.5 eV and 2.7 eV for growth temperatures of 120°C, 100°C, and 90°C respectively. These values are smaller than that of run 3, but are bigger than that of literature and what should be expected using the particle sizes to approximate bandgap[44, 57, 60]. As Wise[44] noted the blueshift confirms the quantum confinement effect that would be desired when synthesizing PbS nanoparticles at diameters that are less than the PbS exciton Bohr radius of 18 nm and fit well with literature theoretical models[57, 60]. The results from runs 4 indicate that the quantum confinement effect would not be as enhanced as literature states when the particle size is smaller than the exciton Bohr radii.

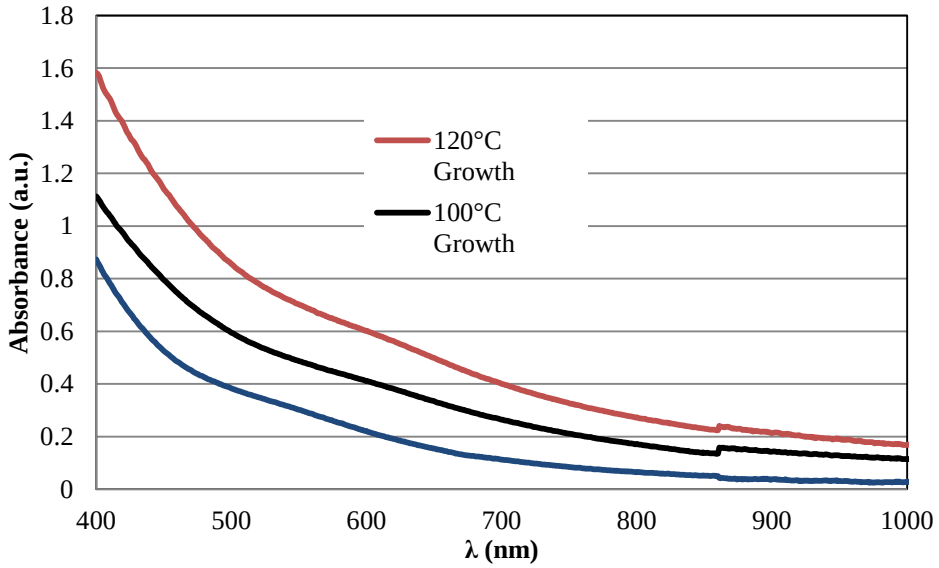

Figure 4.41 UV-Vis results of particles synthesized for run 4

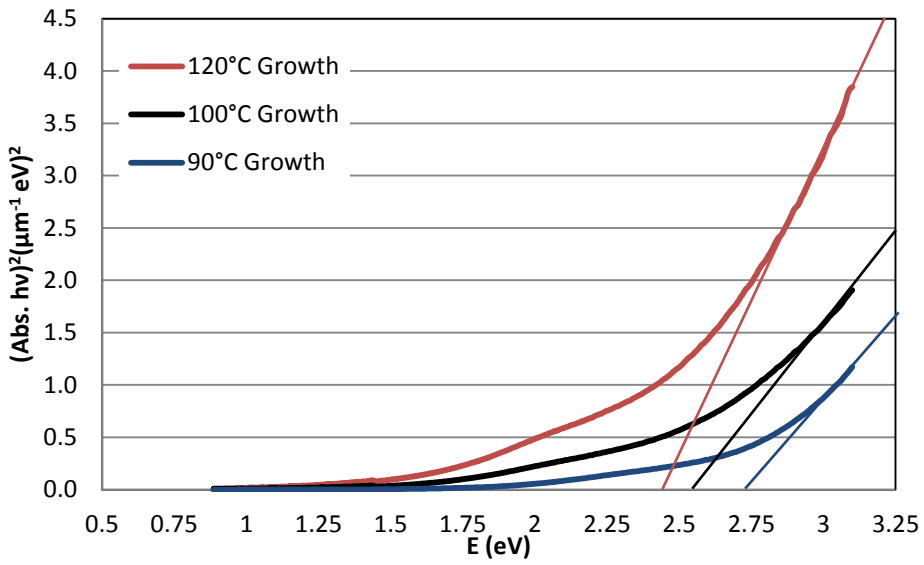

Figure 4.42 Fitted absorbance data for determining bandgap energy when assuming absorbance is zero.

In the synthesis of PbS, approximately spherical particles were synthesized and monodispersion was also accomplished. The added complexity of the $CuInSe_2$ ternary system as compared to the binary PbS system could mean that OA cannot sufficiently control the exchange of active atomic species onto the surface of the nuclei. Uncontrolled growth of nuclei can result in large aggregates. With both the synthesis of PbS and $CuInSe_2$ the reaction parameters of growth temperature, residence time and the concentration of oleic acid which was used as the organic capping surfactant were found to be important in determining growth of nanocrystals and composition. In the synthesis of $CuInSe_2$ the minimum temperature to synthesize nanocrystals was discovered to be about 190°C. In retrospect, additional synthesis runs of growing CuSe nanocrystals followed by an injection of an indium precursor could have been investigated and compared to published work[11, 24]. Future work in synthesizing $CuInSe_2$ nanoparticles is investigation utilizing different solvents in this continuous reaction system[11, 28], using the synthesized material in a device to test the electronic and optical properties, and attempting to scale-up the process to increase production of material to meet application demand.

CHAPTER 5
CONCLUSIONS

5.1 Current State of Topic Research Synthesis

The synthesis work presented here, for PbS, is the first known to use a continuous flow system system process. With $CuInSe_2$, the material set has been well researched using batch methods and the method presented here is a further development upon previously published work in our research group. Other synthesis methods include batch methods or difficult vacuum systems that are costly in terms of capital requirements.

5.2 Summary of Motivation for Topic Research

The motivation for synthesizing binary PbS nanocrystals was to demonstrate the utility of using a continuous flow microreactor system. Previous published work was completed using batch methods which do not readily allow for reaction parameter changes, like those allowed in continuous flow systems. The effect of the reaction parameters of residence time, growth temperature and surfactant concentration on the quality of PbS nanocrystals were the desired outcomes of this work.

An additional proof of concept was to apply binary synthesis methods and parameters to a more difficult ternary ($CuInSe_2$) nanocrystals synthesis. The added complexity of taking precursors to the intermediate binary structures of Cu_xSe_y and In_xSe_y and finally converting these intermediates to the stoichiometric ternary $CuInSe_2$ nanocrystal was investigated for a further proof of concept as applied to more challenging nanocrystal synthesis

5.3 Results and Recommendations of PbS and $CuInSe_2$ Synthesis

The continuous flow nanoparticle reaction scheme for synthesizing PbS and $CuInSe_2$ of quality shape, size and composition was successful. Synthesis runs for PbS nanocrystals elucidated important information concerning the reaction parameters of growth temperature, residence time and the concentration of oleic acid (which was used as the organic capping surfactant). With a molar ratio of 32:2:1 of OA:Pb:S, particle sizes ranging from 7nm to 20nm were synthesized with XRD results indicating the proper peak fingerprint for PbS nanocrystals. The sizes of the particles were found to be dependent upon the growth temperature and residence time within the growth zone of the continuous flow system. As growth temperature and/or residence time increased, the particle size increased as well. Upon changing the concentration of OA, to a molar ratio of 4:2:1 of OA:Pb:S, the particle sizes ranged from about 3.5nm to 7nm. It was found that the particles are not as adequately capped with the 4:2:1 molar ratio due to results showing an increased lack of shape uniformity of the nanocrystals. At the 32:2:1 molar ratio the particles appeared to be more uniform in shape owing to the OA, at high concentrations, helping form the desired 20 nm PbS cubic shape monocrystalline nanocrystals.

Optical characterization of experiment run nanocrystals provided for absorption onsets and excitation results that compared well with published work, but when determining the bandgap energies the results varied between the individual runs and also differed from those given in published work. Although solution based optical characterization can help in determining optical properties of materials, the thought is that the solvents and how well the particles are dispersed in the solvent, size of nanocrystals and size distribution are important for obtaining desired results from the characterization techniques. However, these materials are used in commercial applications in a film-solid-dry-state, not in a suspended solution. Given this fact, further optical characterization, that is not solution based, may be needed to determine if the physical properties of synthesized materials are actually as enhanced

as published works state, concerning the magnitude of the quantum confinement effect.

Synthesis runs for $CuInSe_2$ nanocrystals provided further confirmation as to the importance of growth temperature, residence time and surfactant concentration for the final nanocrystal size and composition. Once again growth temperature was important for crystal growth, but was also found to be important in converting the binary intermediates of Cu_xSe_y and In_xSe_y into the desired ternary $CuInSe_2$ nanocrystal. At lower temperature runs, XRD results showed that intermediates were present, but were converted to $CuInSe_2$ when a 250°C temperature was used. Residence time also contributed to how much the intermediates were converted to $CuInSe_2$. Unlike the synthesis of PbS, synthesizing $CuInSe_2$ presented problems with formed particle agglomeration in all runs. The thought is that with the $CuInSe_2$ system, that OA may not be a sufficiently active surfactant for use with the added complexity of this ternary structure. As a ligand source, OA has been shown to be a more weakly binding surfactant when compared to other ligands and with $CuInSe_2$ this seems to be a problem when monodispersed particles are desired. Due to being a weakly binding ligand on the surface (or not providing complete coverage of the surface) of the $CuInSe_2$ nanocrystals, the synthesized particles seem to have a Van der Waals like attraction for one another which caused the persistent agglomeration results.

Another important factor that contributes to the final quality of the nanocrystals obtained is that a proper washing method is needed. As was seen with the $CuInSe_2$ synthesis, when a rigorous washing method was applied the appearance of removing precursors and/or reaction by products was evident.

A last comment needs to be added about the process equipment materials used for the synthesis runs. When stainless steel pump heads and tubing were used for the PbS and $CuInSe_2$ synthesis, impurities were present when XRD characterization was completed those synthesized materials. When the precursors are converted to the active atomic species, the aggressive reaction by products were

found, including active chlorinated compounds that readily react with the stainless steel process equipment.

5.4 Recommendations for Future Development

The results presented in this work provide insight into the effects that growth temperature, residence time and surfactant concentration have on the synthesis of PbS and $CuInSe_2$ nanocrystals using a continuous flow system system. Other factors such as post-processing of the synthesized materials and material composition of the reactor system tubing and pumps were also important.

In order to further advance the continuous flow synthesis system for nanocrystal production, process scale-up research is needed. For this work, the total flowrates were between 0.5 mL/min to 1.0 mL/min with PbS or $CuInSe_2$ being produced at about 10 mg/min to 20 mg/min. By increasing throughput, additional problems may arise if converted materials are not of the desired size, shape or composition. Scaling-up the continuous process is needed in order to produce nanocrystals at sufficient quantities to meet application demands for solar cells, optical devices and biological sensing applications.

In the case of $CuInSe_2$ synthesis, changing the ligand from OA to a ligand such as oleylamine or TOPO is needed in order to investigate if dispersed particles can be synthesized with a stronger binding ligand. As was shown with using OA as a ligand, the particles synthesized were highly agglomerated. By using a ligand that binds more strongly to the surface of the nanocrystal, the particles can grow in a more monocrystalline manner. Another recommendation would be to investigate the feasibility of first synthesizing CuSe nanocrystals followed by injection of an indium precursor for the synthesis of $CuInSe_2$ nanocrystals. This approach might offer a better control over the stoichiometry of $CuInSe_2$ nanocrystals in a continuous flow system system. The last recommendation would be to separate the nucleation and growth zones. Nucleating at 250°C followed by growth at temperatures below

250°C can allow for more controlled growth and/or understand of the conversion of precursors to active atomic species with the recipe being used.

With PbS synthesis, a recommendation for future work would be better separation of the nucleation and subsequent growth zones. Due to limitations with the continuous flow setup used, separation of the nucleation and growth zone was limited. Being able to have distinct zones for both nucleation and growth would help determine how well the particles nucleate at different injection temperatures and also how much of the particle size is due to the growth zone conditions. For example, if most of the particle size characteristics are due to the nucleation event, then the capital requirements for the growth zone can be reduced. Another recommendation would be to investigate making the synthesis method more environmentally friendly. Chemicals used are highly toxic and improving the chemicals can help alleviate toxic waste and also make working environments safer.

The final recommendation is to apply the synthesized PbS or $CuInSe_2$ nanocrystals in a functional solar cell or LED. The main motivation for synthesizing the materials presented in this work was to make nanocrystals that are suitable for functional device applications. As the particles become increasingly smaller than the exciton Bohr radius, the electronic and optical properties of the particles show quantum confinement effect. Placing PbS or $CuInSe_2$ nanocrystals into a device will help to determine how significant the enhancement due to the quantum confinement effect actually is. A significant enhancement of these properties will validate the need to produce nanocrystals in sizes that are less than 10 nm, whereas minimal enhancements would focus further synthesis research on crystals that are larger and much easier produce.

BIBLIOGRAPHY

1. Jin, H. D. Continuous and Rapid Synthesis of Nanoclusters and Nanocrystals using Scalable Microstructured Reactors. Oregon State University, 2010.
2. Buhro, W. E.; Colvin, V. L. *Nature Materials* **2003,** 2, (3), 138-139.
3. Yin, Y.; Alivisatos, A. P. *Nature* **2005,** 437, (7059), 664-670.
4. Alivisatos, A. P. *Journal of Physical Chemistry* **1996,** 100, (31), 13226-13239.
5. Machol, J. L.; Wise, F. W.; Patel, R. C.; Tanner, D. B. *Physical Review B* **1993,** 48, (4), 2819-2822.
6. Zhong, H. Z.; Li, Y. C.; Ye, M. F.; Zhu, Z. Z.; Zhou, Y.; Yang, C. H.; Li, Y. F. *Nanotechnology* **2007,** 18, (2).
7. Castro, S. L.; Bailey, S. G.; Raffaelle, R. P.; Banger, K. K.; Hepp, A. F. *Chemistry of Materials* **2003,** 15, (16), 3142-3147.
8. Akhtar, J.; Malik, M. A.; O'Brien, P.; Wijayantha, K. G. U.; Dharmadasa, R.; Hardman, S. J. O.; Graham, D. M.; Spencer, B. F.; Stubbs, S. K.; Flavell, W. R.; Binks, D. J.; Sirotti, F.; El Kazzi, M.; Silly, M. *Journal of Materials Chemistry* **2010,** 20, (12), 2336-2344.
9. Malik, M. A.; O'Brien, P.; Revaprasadu, N. *Advanced Materials* **1999,** 11, (17), 1441-1444.
10. Allen, P. M.; Bawendi, M. G. *Journal of the American Chemical Society* **2008,** 130, (29), 9240-+.
11. Arici, E.; Hoppe, H.; Schaffler, F.; Meissner, D.; Malik, M. A.; Sariciftci, N. S. *Applied Physics a-Materials Science & Processing* **2004,** 79, (1), 59-64.
12. Kar, M.; Agrawal, R.; Hillhouse, H. W. *Journal of the American Chemical Society* **2011,** 133, (43), 17239-17247.
13. Luo, Y. L. *Colloid Journal* **2009,** 71, (3), 375-379.
14. Tang, J.; Hinds, S.; Kelley, S. O.; Sargent, E. H. *Chemistry of Materials* **2008,** 20, (22), 6906-6910.
15. Hines, M. A.; Scholes, G. D. *Advanced Materials* **2003,** 15, (21), 1844-1849.
16. Zhong, H. Z.; Wang, Z. B.; Bovero, E.; Lu, Z. H.; van Veggel, F.; Scholes, G. D. *Journal of Physical Chemistry C* **2011,** 115, (25), 12396-12402.
17. Chang, C.-H.; Ting, J.-M. *Thin Solid Films* **2009,** 517, (14), 4174-4178.
18. Chen, H.; Yu, S. M.; Shin, D. W.; Yoo, J. B. *Nanoscale Research Letters* **2010,** 5, (1), 217-223.
19. Jiang, Y.; Wu, Y.; Mo, X.; Yu, W. C.; Xie, Y.; Qian, Y. T. *Inorganic Chemistry* **2000,** 39, (14), 2964-+.
20. Xiao, J. P.; Xie, Y.; Xiong, Y. J.; Tang, R.; Qian, Y. T. *Journal of Materials Chemistry* **2001,** 11, (5), 1417-1420.
21. Bensebaa, F.; Durand, C.; Aouadou, A.; Scoles, L.; Du, X.; Wang, D.; Le Page, Y. *Journal of Nanoparticle Research* **2010,** 12, (5), 1897-1903.
22. Koo, B.; Patel, R. N.; Korgel, B. A. *Journal of the American Chemical Society* **2009,** 131, (9), 3134-+.
23. Panthani, M. G.; Akhavan, V.; Goodfellow, B.; Schmidtke, J. P.; Dunn, L.; Dodabalapur, A.; Barbara, P. F.; Korgel, B. A. *Journal of the American Chemical Society* **2008,** 130, (49), 16770-16777.

24. Guo, Q.; Kim, S. J.; Kar, M.; Shafarman, W. N.; Birkmire, R. W.; Stach, E. A.; Agrawal, R.; Hillhouse, H. W. *Nano Letters* **2008,** 8, (9), 2982-2987.
25. Li, B.; Xie, Y.; Huang, J. X.; Qian, Y. T. *Advanced Materials* **1999,** 11, (17), 1456-1459.
26. Liu, H.; Jin, Z.; Wang, W.; Li, J. *Crystengcomm* **2011,** 13, (24), 7198-7201.
27. Merino, J. M.; deVidales, J. L. M.; Mahanty, S.; Diaz, R.; Rueda, F.; Leon, M. *Journal of Applied Physics* **1996,** 80, (10), 5610-5616.
28. Wark, S. E.; Hsia, C.-H.; Luo, Z.; Son, D. H. *Journal of Materials Chemistry* **2011**.
29. Kim, K. H.; Chun, Y. G.; Park, B. O.; Yoon, K. H. *Designing, Processing and Properties of Advanced Engineering Materials, Pts 1 and 2* **2004,** 449-4, 273-276.
30. Chang, J.; Han, J. E.; Jung, D.-Y. *Bulletin of the Korean Chemical Society* **2011,** 32, (2), 434-438.
31. Lee, C.-H.; Wu, C.-H.; Lu, C.-H. *Journal of the American Ceramic Society* **2010,** 93, (7), 1879-1883.
32. Lee, J. S.; Suryanarayana, I.; Lee, H.-Y.; Hwang, Y. K.; Chang, J.-S. *Journal of Nanoscience and Nanotechnology* **2010,** 10, (1), 303-308.
33. Wu, C.-C.; Shiau, C.-Y.; Ayele, D. W.; Su, W.-N.; Cheng, M.-Y.; Chiu, C.-Y.; Hwang, B.-J. *Chemistry of Materials* **2010,** 22, (14), 4185-4190.
34. Grisaru, H.; Palchik, O.; Gedanken, A.; Palchik, V.; Slifkin, M. A.; Weiss, A. M. *Inorganic Chemistry* **2003,** 42, (22), 7148-7155.
35. Eberspacher, C.; Fredric, C.; Pauls, K.; Serra, J. *Thin Solid Films* **2001,** 387, (1-2), 18-22.
36. Kumar, D.; Agarwal, G.; Tripathi, B.; Vyas, D.; Kulshrestha, V. *Journal of Alloys and Compounds* **2009,** 484, (1-2), 463-466.
37. Yang, J. P.; Fendler, J. H. *Journal of Physical Chemistry* **1995,** 99, (15), 5505-5511.
38. Zhao, X. K.; Yang, J.; McCormick, L. D.; Fendler, J. H. *Journal of Physical Chemistry* **1992,** 96, (24), 9933-9939.
39. Wang, Z.; Zhao, B.; Zhang, F.; Mao, W. P.; Qian, G. D.; Fan, X. P. *Materials Letters* **2007,** 61, (17), 3733-3735.
40. Tanino, H.; Maeda, T.; Fujikake, H.; Nakanishi, H.; Endo, S.; Irie, T. *Physical Review B* **1992,** 45, (23), 13323-13330.
41. Rincon, C.; Ramirez, F. J. *Journal of Applied Physics* **1992,** 72, (9), 4321-4324.
42. Zaretskaya, E. P.; Gremenok, V. F.; Riede, V.; Schmitz, W.; Bente, K.; Zalesski, V. B.; Ermakov, O. *Journal of Physics and Chemistry of Solids* **2003,** 64, (9-10), 1989-1993.
43. Bodnar, I. V.; Gurin, V. S.; Molochko, A. P.; Solovei, N. P. *Inorganic Materials* **2004,** 40, (8), 797-801.
44. Wise, F. W. *Accounts of Chemical Research* **2000,** 33, (11), 773-780.
45. Dong, L. H.; Chu, Y.; Zhuo, Y. J.; Zhang, W. *Nanotechnology* **2009,** 20, (12).
46. Lee, S. M.; Jun, Y. W.; Cho, S. N.; Cheon, J. *Journal of the American Chemical Society* **2002,** 124, (38), 11244-11245.
47. Jiang, Y.; Wu, Y.; Xie, B.; Yuan, S. W.; Liu, X. M.; Qian, Y. T. *Journal of Crystal Growth* **2001,** 231, (1-2), 248-251.
48. Duan, T.; Lou, W.; Wang, X.; Xue, Q. *Colloids and Surfaces a-Physicochemical and Engineering Aspects* **2007,** 310, (1-3), 86-93.
49. Jang, S. Y.; Song, Y. M.; Kim, H. S.; Cho, Y. J.; Seo, Y. S.; Jung, G. B.; Lee, C.-W.; Park, J.; Jung, M.; Kim, J.; Kim, B.; Kim, J.-G.; Kim, Y.-J. *ACS Nano* **2010,** 4, (4), 2391-2401.

50. Nagel, M.; Hickey, S. G.; Fromsdorf, A.; Kornowski, A.; Weller, H. *Zeitschrift Fur Physikalische Chemie-International Journal of Research in Physical Chemistry & Chemical Physics* **2007,** 221, (3), 427-437.
51. Deng, D. W.; Zhang, W. H.; Chen, X. Y.; Liu, F.; Zhang, J.; Gu, Y. Q.; Hong, J. M. *European Journal of Inorganic Chemistry* **2009**, (23), 3440-3446.
52. Kumar, A.; Jakhmola, A. *Langmuir* **2007,** 23, (6), 2915-2918.
53. Mo, M. S.; Shao, M. W.; Hu, H. M.; Yang, L.; Yu, W. C.; Qian, Y. T. *Journal of Crystal Growth* **2002,** 244, (3-4), 364-368.
54. Huang, N. M.; Shahidan, R.; Khiew, P. S.; Peter, L.; Kan, C. S. *Colloids and Surfaces a-Physicochemical and Engineering Aspects* **2004,** 247, (1-3), 55-60.
55. Zhou, H. S.; Honma, I.; Komiyama, H.; Haus, J. W. *Journal of Physical Chemistry* **1993,** 97, (4), 895-901.
56. Nikolaeva, E. V.; Ozerin, S. A.; Grigoriev, A. E.; Griogoriev, E. I.; Chvalun, S. N.; Gerasimov, G. N.; Trakhtenberg, L. I. *Materials Science & Engineering C-Biomimetic and Supramolecular Systems* **1999,** 8-9, 217-223.
57. Abel, K. A.; Shan, J.; Boyer, J.-C.; Harris, F.; van Veggel, F. C. J. M. *Chemistry of Materials* **2008,** 20, (12), 3794-3796.
58. Zhou, G. J.; Lu, M. K.; Xiu, Z. L.; Wang, S. F.; Zhang, H. P.; Zhou, Y. Y.; Wang, S. M. *Journal of Physical Chemistry B* **2006,** 110, (13), 6543-6548.